Food & Function

ROYAL SOCIETY OF CHEMISTRY

PAPER

View Article Online
View Journal | View Issue

Cite this: *Food Funct.*, 2026, **17**, 5598

Oleuropein and hydroxytyrosol enhance mitochondrial function and biogenesis in SH-SY5Y cells through estrogen-like mechanisms

Manuela Leri,[a] Daniele Nosi,[b] Diletta Ami,[c] Federica Bovio,[c] Matilde Forcella,[c] Federica Carnemolla,[a] Paolo Mereghetti,[d] Paola Fusi,[c,e] Antonino Natalello,[c] Massimo Stefani,[a] Niccolò Taddei[a] and Monica Bucciantini *[a]

Age-related hormonal and metabolic changes critically increase vulnerability of neurons to neurodegeneration and cognitive decline. Estrogens are known to support neuronal survival, synaptic plasticity, and mitochondrial function, yet hormone replacement therapies have shown inconsistent neuroprotective outcomes. Safe alternatives are therefore highly desirable. In this study, we characterize Oleuropein aglycone (OleA) and hydroxytyrosol (HT), two of the main bioactive phenolic compounds found in extra virgin olive oil (EVOO), as multitarget neuromodulators with estrogen-like and neuroprotective potential. Unlike most studies on phytoestrogens, which have focused on single pathways such as estrogen receptor activation, our findings reveal a broader spectrum of actions. OleA and HT simultaneously modulate ERβ and IGF1R signaling, regulate Ca^{2+} dynamics through ryanodine, AMPA, and NMDA receptors, remodel the neuronal lipidome, and promote mitochondrial biogenesis and metabolic efficiency. Moreover, they influence amyloid-binding alcohol dehydrogenase (ABAD) expression, a mitochondrial target implicated in Alzheimer's disease. By converging on receptor signaling, lipid metabolism, and mitochondrial function, these compounds provide a systems-level perspective on neuronal protection. This multitarget activity, which mimics estrogen-like signaling, positions the investigated EVOO-derived phenolic compounds as safe dietary agents to counteract the neuronal decline associated with estrogen loss during ageing.

Received 14th January 2026,
Accepted 25th May 2026

DOI: 10.1039/d6fo00178e

rsc.li/food-function

1. Introduction

Estrogens, and particularly 17b-estradiol (17b), are widely recognized as central regulators of neuronal survival, synaptic plasticity, and metabolic homeostasis in the brain.[1] Although classically associated with reproductive physiology, estrogens exert profound effects on neuronal function through the modulation of intracellular pathways that govern mitochondrial activity, Ca^{2+} dynamics, inflammatory responses, and overall cellular homeostasis.[2,3] In the hippocampus, 17b enhances acetylcholine synthesis and neuronal communication,[4] promotes dendritic spine formation and the expression of neurotrophic mediators such as brain-derived neurotrophic factor (BDNF),[5] and finely tunes the activity of α-amino-3-hydroxy-5-methyl-4-isoxazole propionic acid (AMPA) and *N*-methyl-D-aspartate (NMDA) receptors, which are essential for neuronal excitability, synaptic transmission, and plasticity.[6] In parallel, 17b sustains mitochondrial function and limits oxidative stress, thereby supporting long-term neuronal viability.[2]

These neuroprotective actions derive from the integration of genomic and rapid membrane-initiated signaling mechanisms.[3,7] In the "classical" genomic pathway, 17b binds estrogen receptors (ERα and ERβ), which translocate to the nucleus and function as transcriptional regulators orchestrating long-term adaptive responses.[7,8] At the same time, by "non-classical" pathway, membrane-associated ERs trigger rapid signaling cascades involving Ca^{2+} fluxes and activation of mitogen-activated protein kinase (MAPK) pathways. Among MAPK members, extracellular signal-regulated kinase (ERK1/2) plays a critical role in synaptic plasticity, mitochondrial signaling, and activity-dependent transcriptional regulation.[9] These rapid events promote phosphorylation of downstream effectors such as cAMP response element-binding protein (CREB), enabling modulation of gene expression on a faster timescale

[a]*Department of Experimental and Clinical Biomedical Sciences, University of Florence, Viale Morgagni 50, 50134 Florence, Italy.*
E-mail: monica.bucciantini@unifi.it; Tel: +39 0552751250
[b]*Department of Experimental and Clinical Medicine, University of Florence, Florence, Italy*
[c]*Department of Biotechnology and Biosciences, University of Milano-Bicocca, Piazza della Scienza, 2, 20126 Milano, Italy*
[d]*Bioinformatics Consultant, 15061 Arquata Scrivia, Italy*
[e]*MISTRAL, Interuniversity Research Centre "Integrated Models of Study for Health Protection and Prevention in Living and Working Environments", University of Brescia, Milano-Bicocca and Verona, Italy*

as compared with the classical genomic mechanism.[10] The importance of these receptors is underscored by evidence showing that disruption of ER signaling markedly reduces the neuroprotective efficacy of 17b. ERβ has attracted considerable attention for its involvement in mitochondrial regulation and neuronal resilience.[11,12]

Estrogen signaling operates within a broader network of trophic pathways. Rapid estrogen responses intersect with insulin-like growth factor 1 receptor (IGF1R) signaling, reinforcing neuronal survival and metabolic adaptation.[13] Activation of IGF1R-dependent PI3K/Akt signaling contributes to mitochondrial integrity and bioenergetic remodeling.[14] The convergence of Ca^{2+} signaling, ER activation, ERK1/2 phosphorylation, and IGF1R-mediated pathways highlight the integrated and multilayered nature of estrogen-driven neurotrophic responses.

At the mitochondrial level, estrogens regulate key determinants of biogenesis and genome stability, including PGC-1α, a master controller of mitochondrial DNA replication and transcription.[15] They also interact with mitochondrial-associated proteins such as amyloid-binding alcohol dehydrogenase (ABAD), a mitochondrial enzyme capable of binding amyloid-β and implicated in redox imbalance, mitochondrial dysfunction, and neurodegenerative processes.[16] Collectively, these mechanisms define an estrogen-sensitive regulatory network that links receptor activation to mitochondrial remodeling and cellular bioenergetics.

The age-related decline in estrogen levels has been associated with increased vulnerability to neurodegenerative disorders, including Alzheimer's and Parkinson's diseases.[17,18] Although hormone replacement therapy (HRT) has been explored as a strategy to counteract estrogen loss, its clinical benefits remain debated and appear highly dependent on timing, formulation, and individual risk profiles.[19] These uncertainties have stimulated growing interest in alternative approaches capable of modulating estrogen-related pathways while avoiding the potential risks associated with prolonged hormonal treatment.

In this context, dietary bioactive compounds have emerged as promising modulators of estrogen-sensitive signaling networks. Phytoestrogens such as soy isoflavones act as partial ER agonists and often display preferential affinity for ERβ.[20] Genistein, for example, influences neurogenesis, inflammatory signaling, and synaptic plasticity in experimental systems.[21] More broadly, specific classes of plant-derived polyphenols, including flavonoids and secoiridoids, regulate redox balance, mitochondrial function, and metabolic signaling pathways. However, whether specific dietary polyphenols can coordinate estrogen-dependent signaling with mitochondrial remodeling in neuronal cells remains insufficiently understood.

Oleuropein, a secoiridoid glycoside abundant in olive leaves and in extra virgin olive oil (EVOO), together with its derivatives, exhibits well-established anti-inflammatory, antioxidant, and antiproliferative properties.[22,23] Among its bioactive forms, oleuropein aglycone (OleA), and its catecholic metabolite hydroxytyrosol (HT) are major EVOO-derived phenolic compounds. Both have been reported to modulate autophagy, inflammatory signaling and redox balance in both neuronal and glial models;[24,25] nevertheless, their potential interaction with estrogen-related pathways, as well as their capacity to coordinate mitochondrial bioenergetics within an estrogen-like regulatory framework, remains insufficiently explored.

From a nutritional and translational perspective, bioavailability and brain accessibility are critical issues. HT is efficiently absorbed after dietary intake and circulates predominantly as sulfate and glucuronide conjugates at low micro- to sub-micromolar concentrations, whereas the free form is present at much lower levels.[26,27] Importantly, experimental evidence indicates that HT and/or its metabolites are capable of crossing the Blood-Brain Barrier (BBB) and can be detected in brain tissue, although at relatively low concentrations whose precise levels remain incompletely defined,[26,28–30]. In contrast, OleA is extensively metabolized, with HT representing one of its main downstream products. While OleA and its derivatives are systemically detectable,[27] direct evidence supporting the ability of OleA to cross the BBB in its intact form remains limited, and its potential central effects may therefore be mediated, at least in part, by its metabolites.

The present study investigated whether OleA and HT act as integrated estrogen-like modulators in neuronal cells. Using human SH-SY5Y cells, we examined ERβ activation and its association with Ca^{2+} homeostasis, IGF1R signaling, ERK1/2 activation, mitochondrial biogenesis, lipid remodeling, and metabolic reprogramming. Through the integration of imaging analyses, biochemical assays, FTIR microspectroscopy, and Seahorse-based metabolic profiling, we aimed to define the coordinated molecular adaptations induced by these EVOO-derived phenolic compounds.

2. Materials and methods

2.1. Reagents

17b-Estradiol (17b, E2257, purity ≥97% (HPLC)) was obtained from Merck KGaA, Darmstadt, Germany. PHTPP (SML1355) (2-phenyl-3-(4-hydroxyphenyl)-5,7-bis(trifluoromethyl)-pyrazolo [1,5-*a*]pyrimidine,4-[2-phenyl-5,7-bis(trifluoromethyl)pyrazolo [1,5-*a*]-pyrimidin-3-yl]phenol); CNQX (C127) (6-cyano-7-nitroquinoxaline-2,3-dione), and memantine hydrochloride (M9292) (3,5-dimethyl-1-adamantanamine hydrochloride) were also sourced from Merck KGaA, Darmstadt, Germany. Ryanodine (Rya, 559276), 2-aminoethyl diphenylborinate (2-APB, D9754), and (AG 538, T7697) (α-cyano-(3-methoxy-4-hydroxy-5-iodocinnamoyl)-(3′,4′-dihydroxyphenyl)ketone) were provided by the same supplier.

2.2. Cell culture conditions

SH-SY5Y neuroblastoma cells, obtained from ATCC (CRL-2266), were maintained at 37 °C in a humidified incubator with a 5.0% CO_2 atmosphere. Cells were cultured in a 1 : 1 mixture of Ham's F-10 nutrient mixture and Dulbecco's Modified Eagle Medium (DMEM), supplemented with 10% fetal bovine serum (FBS), 3 mM glutamine, 100 units per mL penicillin, and 100 μg mL^{-1} streptomycin.

2.3. Sample preparation and treatments

17b was dissolved in ethanol to achieve a 3.67 mM stock solution and stored at 4 °C. Working solutions (1 mM) were prepared in serum-free medium and stored at −20 °C. Oleuropein, (≥98% HPLC, Extrasynthese Genay, France), was enzymatically deglycosylated using almond β-glucosidase (EC 3.2.1.21, Merck KGaA, Darmstadt, Germany), as previously described.[31] Stock solutions of Oleuropein aglycone (OleA, 50 mM) were maintained frozen, protected from light and utilized immediately after thawing. Hydroxytyrosol (HT ≥98% HPLC, Merck KGaA), was dissolved in aqueous solution (100 mM stock) and stored under conditions minimizing oxidation (low temperature, low ionic strength, low salt content).[32]

Cell treatments were performed in the absence or in the presence of PHTPP (100 nM), a selective ERβ full antagonist, with a PHTPP pre-treatment of 30 min followed by incubation for 4 or 24 h with 10 nM 17b,[33] or with OleA or HT (5 μM and 10 nM).

2.4. Mitochondrial membrane potential evaluation

SH-SY5Y cells (5×10^4 cells per well) cultured on glass coverslips were incubated for 45 min at 37 °C with 500 nM MitoTracker CMXRos (Thermo Fisher) and Hoechst 33342 for nuclear staining. Subsequently, the cells were fixed in 2.0% buffered paraformaldehyde for 10 min, washed in PBS, and mounted on microscope slides with Fluoromount™ Aqueous Mounting Medium (Sigma Aldrich-Merck). Multicolor images were captured using a Leica TCS SP8 scanning microscope equipped with a 63×, 1.4–0.6 NA, oil, HCX Plan APO lens. MitoTracker Red was excited at 561 nm and emission was collected between 580–650 nm, 405 nm diode laser was used for Hoechst 33342. Images were acquired in sequential scanning mode to avoid spectral overlap. Mitochondrial morphology was assessed by analyzing six randomly selected fields using the ImageJ plugin in accordance with established workflows for image pre-processing and analysis.[34]

2.5. Ca^{2+} flux measurement

Intracellular Ca^{2+} levels were observed using the fluorescent probe Fluo-3 acetoxymethyl ester (Fluo-3 AM; Molecular Probes, Thermo Fisher Scientific). Subconfluent SH-SY5Y cells (8×10^4 cells per well) grown on glass coverslips were incubated with 5 μM Fluo-3 AM at 37 °C for 15 min to allow intracellular dye loading, according to the manufacturer's instructions and established protocols for AM-ester Ca^{2+} indicators. Cells were subsequently subjected to the indicated treatments for 30 min or 1 h. The cells were fixed in 2.0% paraformaldehyde in PBS for 10 min. Intracellular Ca^{2+} imaging was performed using a Leica TCS SP8 confocal microscope equipped with fixed laser lines. Fluo-3 AM was excited using the 488 nm Argon laser line and fluorescence emission was collected between 500–550 nm. Nuclei were counterstained with Hoechst 33342, excited with a 405 nm diode laser and detected between 420–480 nm. Images were acquired in sequential scanning mode to avoid spectral overlap. All images were obtained using a 40× oil immersion objective (NA 1.3) under identical laser power and detector gain settings across experimental groups.

Live-cell Ca^{2+} flux was assessed in SH-SY5Y cells plated in 96-well plates (2×10^4 cells per well), labelled with Fluo-3 AM. The fluorescence intensity of Fluo-3 AM was continuously monitored at 526 nm over 2 h following addition to the culture medium of 10 nM 17b, 5 μM and 10 nM OleA and HT using a Biotek Synergy 1H plate reader. Where indicated, cells were pretreated for 60 min with CNQX (5 μM) to inhibit AMPA receptor-mediated signaling,[35] memantine (10 μM) to block NMDA receptor[35] activity, Rya (10 μM) to inhibit ryanodine receptor (RyR)-mediated Ca^{2+} release, or 2-APB (100 μM) to inhibit inositol 1,4,5-trisphosphate receptor (IP_3R)-dependent Ca^{2+} signaling. Rya was used within the inhibitory micromolar range (≥10 μM), known to stabilize the closed/inactivated state of RyR channels and thereby reduce Ca^{2+} release from intracellular stores. 2-APB was applied at 100 μM, a concentration widely used to effectively suppress IP_3R-mediated Ca^{2+} mobilization and store-operated Ca^{2+} entry in cellular models.

2.6. Immunofluorescence

Subconfluent SH-SY5Y cells (8×10^4 cells per well) grown on glass coverslips were subjected to various treatments for 24 h and subsequently washed with PBS. Cells were pretreated for 60 min with 2 μM I-OMe-AG-538, according to the manufacturer's instructions (AG-538; a specific IGF1R tyrosine kinase inhibitor), to block IGF1R autophosphorylation in intact cells, as described in cell-signaling inhibition protocols in which AG-538 at micromolar concentrations inhibits IGF1R phosphorylation and downstream signaling. Cell nuclei were stained with Hoechst 33342 for 30 min at 37 °C. Cell membrane labeling was performed by incubating the cells with 10 ng mL^{-1} CTX-B Alexa488 (C34775, Thermo Fisher Scientific Inc.) in a complete cold medium for 10 min at room temperature. Following fixation in 2.0% buffered paraformaldehyde for 10 min, cells were permeabilized using a 1 : 1 acetone/ethanol solution for 4 min at room temperature, washed with PBS, and blocked with PBS containing 0.5% BSA and 0.2% gelatin. Then the cells were incubated for 1 h at room temperature with primary antibodies: rabbit anti-ERβ primary antibody (1 : 500, Merck KGaA), rabbit PGC-1α (1 : 500, 2178, Cell Signaling), mouse anti-NMDA antibody (1 : 800, MAI-2014, Thermo Fisher Scientific Inc.), mouse AMPA subunit antibody (1 : 800, MAB397, Merck KGaA), rabbit anti-ERAB/ABAD antibody (1 : 500, GTX100301, GeneTex Inc.), and rabbit anti-phospho-IGF1 receptor β (p-IGF1R, 1 : 500, 3024, Cell Signaling Technology) in blocking solution. Following a 30 min washing step with PBS, cells were incubated with secondary antibodies: anti-Rabbit IgG (H + L) Cross-Adsorbed Secondary Antibody Alexa Fluor® 568 conjugate (A-11011, Thermo Fisher Scientific Inc.) or anti-Mouse IgG (H + L) Cross-Adsorbed Secondary Antibody Alexa Fluor® 568 conjugate (A-11004, Thermo Fisher Scientific Inc.), diluted 1 : 200 in PBS. Finally, cells were washed twice in PBS and once in distilled water to eliminate

non-specifically bound antibodies. Images were acquired using a Leica TCS SP8 confocal microscope equipped with fixed laser lines. Fluorophores were excited using a 405 nm diode laser for Hoechst, a 488 nm Argon laser for Alexa Fluor 488, and a 561 nm DPSS laser for Alexa Fluor 568. Emission signals were collected sequentially using the following detection windows: 420–480 nm for Hoechst, 500–550 nm for Alexa Fluor 488, and 580–630 nm for Alexa Fluor 568. All images were acquired using a 63× oil immersion objective (NA 1.4). Images were acquired with Leica LAS-AF imaging software and analyzed using FiJi software.[36]

2.7. Proximity analysis of ERβ and mitochondria

SH-SY5Y cells were treated with 10 nM 17b, 10 nM OleA or HT. Estrogen Receptor β (ERβ) was detected using a rabbit polyclonal anti-ERβ primary antibody (1 : 500, Merck KGaA) alongside an anti-rabbit IgG (H + L) cross-adsorbed secondary antibody, Alexa Fluor™ 514 (1 : 500, A-31558, Thermo Fisher Scientific). Mitochondria were labeled with MitoTracker Red and nuclei with Hoechst 33342. Confocal images were acquired using a Leica STELLARIS microscope equipped with a Plan-Apochromat 63× oil-immersion objective. The acquisition resolution was 0.180 μm in the *XY* plane and 0.300 μm along the *Z* axis. To assess the proximity of ERβ to mitochondria, a probability map of mitochondrial distribution was first generated from the MitoTracker channel using AIVIA software (version 12, DRVision Technologies LLC, Bellevue, WA, USA; https://www.drvtechnologies.com/aivia/). Subsequently, a machine learning model was trained on two channels, ERβ and the previously generated mitochondrial probability map, to detect receptor signals close to the mitochondrial structures. Training regions included portions of the ERβ and mitochondrial clusters, adjacent cytoplasmic areas, and potential overlapping zones. The proximity threshold was defined as ≤0.2 μm. The model was then applied to the entire dataset to detect and classify ERβ signals in proximity to mitochondria across the image stack. On the resulting ERβ probability map, approximately 120 volumes of interest (VOIs) were manually selected across ~20 cells per acquisition volume using the segmentation tools provided by the AIVIA software. A threshold intensity value of 50 (equivalent to 25% receptor probability) was applied to include only receptor signals above this cutoff in each VOI. Quantification of the receptor signal was performed by measuring the integrated density within each VOI. Statistical analysis was conducted using Jamovi (version 2.4; https://www.jamovi.org).

2.8. STED confocal microscopy

Subconfluent SH-SY5Y cells were cultured on glass coverslips at a density of 8×10^4 cells per well. Following treatment, the cells were stained with 0.01 mg mL^{-1} wheat germ agglutinin, Tetramethylrhodamine Conjugate (TMR, W849, Thermo Fisher Scientific). Estrogen Receptor β (ERβ) was detected using a rabbit polyclonal anti-ERβ primary antibody (1 : 500, Merck KGaA) alongside an anti-rabbit IgG (H + L) cross-adsorbed secondary antibody, Alexa Fluor™ 514 (1 : 500, A-31558, Thermo Fisher Scientific). Fluoromount-G™ (Thermo Fisher Scientific) served as the mounting medium. STED images were acquired using a Leica SP8 STED 3× confocal microscope (Leica Microsystems) equipped with a white light laser (WLL) and a pulsed 660 nm depletion laser. The following excitation wavelengths were used: 405 nm for Hoechst 33342, 514 nm for Alexa Fluor 514, and 561 nm for WGA–TMR. Emission signals were collected sequentially using the following detection windows: 420–480 nm for Hoechst, 520–560 nm for Alexa Fluor 514, and 580–630 nm for TMR. Images were collected using the Leica LAS-AF image acquisition software and processed with FiJi software.[36]

2.9. Western blotting

SH-SY5Y cells (1×10^5 cells per well) were plated in a 6-well plate and incubated for 24 h before various treatments. Subsequently, the cells were washed with cold PBS, lysed in 80 μL of Laemmli buffer (62.5 mM Tris-HCl, pH 6.8, 10% (w/v) SDS, 25% (w/v) glycerol) without bromophenol blue. Whole cell lysates were collected, boiled at 95 °C for 10 min, and centrifuged at 12 000*g* for 10 min at 4 °C. The total protein concentration was determined using the BCA assay. A total of 25 μg of protein was loaded onto precast SDS-PAGE gels (Bio-Rad) and subsequently transferred to a PVDF membrane using the trans-Blot Turbo Transfer Pack (Bio-Rad). Immunoblots were incubated at room temperature in PBS containing 5.0% (w/v) BSA and 0.1% (v/v) Tween-20, and were probed with primary antibodies specific for GSK3β (9832, Cell Signaling Technology), phospho-GSK3β (Ser9) (5558, Cell Signaling Technology), ERAB/ABAD (1 : 500, GTX100301, GeneTex Inc.), phospho-ERK1 (Thr202/Tyr204)/phospho-ERK2 (Thr185/Tyr187) (GTX132783, GeneTex, Inc.), ERK1/2 (GTX134462, GeneTex, Inc.), and GAPDH (97166, Cell Signaling Technology). Following the incubation with primary antibody, the membranes were treated with 1 : 5000 diluted HRP-conjugated anti-rabbit or anti-mouse secondary antibodies (7074 and 7076, Cell Signaling Technology). The membranes were washed multiple times with PBS containing 0.5% (v/v) Tween®-20, and protein bands were detected using Clarity Western ECL solution. Chemiluminescent signals were captured with the Amersham™ 600 Imager imaging system (GE Healthcare Life Science, Pittsburgh, PA, USA), and densitometric analysis was performed using FiJi software.[36]

2.10. FTIR microspectroscopy analysis of intact SH-SY5Y cells

FTIR microspectroscopy measurements have been performed on intact SH-SY5Y cells exposed to 17b, OleA or HT for 24 h. In brief, SH-SY5Y cells were seeded at 1×10^6 cells per 100 mm dish and the following day were treated with 10 nM 17b, 10 nM or 5 μM OleA and 10 nM or 5 μM HT in starvation for 24 h. As a control, we also measured untreated cells. Twenty-four h after the treatment, the cells were harvested by trypsinization and washed three times in physiological solution (NaCl 0.9%), by centrifugation at 300*g* for 5 min to eliminate medium contamination; the resulting pellet has been used for IR measurements.

A few μl of the cell suspension were deposited onto an IR transparent BaF_2 window and dried at room temperature for about 30 min to eliminate the excess water.

Mid-IR absorption spectra were acquired in transmission mode in the 4000–800 cm^{-1} spectral range, by a Varian 610-IR infrared microscope equipped with a mercury cadmium telluride nitrogen-cooled detector and coupled to the Varian 670-IR FTIR spectrometer (Varian Australia Pty Ltd, Mulgrave VIC, Australia). The IR absorption spectra were collected through a microscope diaphragm aperture of 100 μm × 100 μm, working at 2.0 cm^{-1} spectral resolution, 25 kHz scan speed, triangular apodization, and by the accumulation of 512 scan co-additions.

For each sample, different areas were measured to explore possible heterogeneity. Three independent experiments were carried out to evaluate results reproducibility.

Raw spectra have been corrected for water vapor, when necessary, and normalized at the Amide I band area. After a 13-point smoothing, the second derivative spectra were calculated by the Savitzky–Golay method (3rd polynomial, 9 smoothing points). Spectral analysis was performed by GRAMS/32 software (Galactic Ind. Corp., Salem, NH, USA).

2.11. Multivariate and univariate analyses of FTIR spectra

FTIR second derivative spectra were split into four spectral regions and the Partial Least Squares-Discriminant Analysis (PLS-DA) has been applied on each range, as previously described.[37] PLS-DA is a widely used variant of the partial least squares method. In this case, the categorical variable (the classes) describes the treatments and the concentrations. To improve prediction accuracy and to avoid over-fitting, three-time repeated 5-fold cross-validation was applied.[38] Details regarding the applied cross-validation method have been described previously.[39] The best model was selected using the "one standard error rule". In this case, the model with the best performance value (root mean square error) is identified and, using resampling, we can estimate the standard error of performance.[40] The final model used was the simplest model within one standard error of the empirically best model.[37] To assess the importance of each variable (wavenumbers), the weighted sums of the absolute PLS-DA regression coefficients were used. Each PLS-DA model includes the following classes: CTRL, 17b, OleA 10 nM, OleA 5 μM, HT 10 nM, HT 5 μM. Different models have been created considering only some of the classes. Model1: OleA10nM-CTRL-17b, Model2: OleA5μM-CTRL-17b, Model3: HT10nM-CTRL-17b, Model4: OleA5μM-CTRL-17b. The discrimination accuracy among the classes was evaluated using the classification accuracy, *e.g.* the proportion of true results (true positive + true negative) over the total number of samples.

The intensities of a set of selected wavenumbers were used as independent variables to perform a linear discriminant analysis (LDA). The LDA model includes the following classes: CTRL, OleA at 10 nM, OleA at 5 μM, HT at 10 nM, HT at 5 μM and 17b. The discrimination accuracy among the classes was evaluated using the classification accuracy, *e.g.* the proportion of true results (true positive + true negative) over the total number of samples. To quantify the difference between the CTRL and the treatments, the Euclidean distance between all pairs of spectra (in the low dimensional LDA score space) was computed, using the CTRL as reference.

$$D_{K,i,j} = \frac{1}{L}\sqrt{\sum_{c=1}^{L}\left(x_{K,j,c} - r_{i,c}\right)^2}$$

where $r_{i,c}$ is the i-th spectra belonging to the reference group (CTRL), while $x_{K,j,c}$ is the j-th spectra belonging to the treated groups at each point, *e.g.* K = [OleA 10 nM, OleA 5 μM, HT 10 nM, HT 5 μM, 17b]. L is the number of LDA scores and c is the c-th LDA component. A t-test ($\mu = 0$) with Bonferroni correction for multiple comparisons was performed to assess whether the distances were significantly different from 0 (details in Table S1). Moreover, unbalanced one-way ANOVA followed by pairwise comparisons with Tukey's multiple comparison correction was applied to LDA derived Euclidean distances in order to compare the differences among the groups (details in Table S2). ANOVA tests whether mean differences among groups are likely to have occurred by chance.[41]

2.12. Seahorse analysis

The effect of 17b, OleA and HT on SH-SY5Y energy metabolism was investigated through Seahorse technology. The cells were seeded in Agilent Seahorse 96-well XF cell culture microplates at a density of 4×10^4 cells per well in 180 μL of growth medium and allowed to adhere for 24 h in a 37 °C humidified incubator with 5% CO_2. The following day the seeded cells were treated with 10 nM 17b, 10 nM or 5 μM OleA and 10 nM or 5 μM HT in starvation and 24 h after the treatment Agilent Seahorse XF Glycolysis Stress Test, XF Cell Energy Phenotype Test and XF ATP Rate Assay kit were performed according to manufacturer instructions. In addition, before running the assay, the Seahorse XF Sensor Cartridge was hydrated and calibrated with 200 μL of Seahorse XF Calibrant Solution in a non-CO_2 37 °C incubator to remove CO_2 from the media. Each experiment was performed in technical quadruplicate for each treatment and at least three independent biological replicates were carried out. Data were normalized to total protein content, as quantified by Bradford assay.[42] All the kits and reagents were purchased by Agilent Technologies (Santa Clara, CA, USA).

2.13. Statistical analysis

Statistical analysis was performed using one-way or two-way analysis of variance (ANOVA), as appropriate. Two-way ANOVA was used to evaluate the effects of compound (HT *vs.* OleA) and dose, as well as their interaction, while one-way ANOVA was applied to compare treatment groups with CTRL or 17b samples. Multiple comparisons were carried out using Tukey's honestly significant difference (HSD) *post hoc* test. All analyses were performed using OriginPro software, with statistical significance set at $p < 0.05$.

3. Results

3.1. EVOO-derived phenolic compounds induce estrogen receptor expression and nuclear localization

We first investigated the ability of phenolic secoiridoid derivative OleA and the catecholic phenolic alcohol HT to modulate the estrogen receptor beta (ERβ). Human neuroblastoma SH-SY5Y cells were treated for 4 and 24 hours with 10 nM 17b, as previously reported,[43] as well as with OleA and HT at two concentrations: 10 nM, to match the reported concentration of 17b, and 5 μM, to evaluate potential effects at higher concentrations. Our results showed that both 17b and each compound's treatment increased ERβ expression in a time- and concentration-dependent manner, as determined by immunofluorescence assays. Notably, HT at both concentrations tested increased ERβ expression by approximately 2.5-fold compared to untreated cells (CTRL), a response comparable to that induced by 17b (Fig. 1A and C). OleA showed a dose-dependent effect, producing an approximately three-fold increase over CTRL at the highest concentration tested (Fig. 1A and C). This increase was abrogated in the presence of the ERβ antagonists PHTPP (Fig. 1B and C). Furthermore, ERβ nuclear translocation was assessed by 3D reconstruction of cells acquired using STED confocal microscopy (Fig. 2A and B). Images and quantification at 4 h and 24 h showed that OleA (10 nM) induced significantly higher ERβ nuclear localization than 17b at both time points, whereas OleA (5 μM) exhibited a stronger effect than the lower concentration only after 24 h. In contrast, HT produced a milder, dose-dependent increase, suggesting that OleA is a more potent modulator of nuclear ERβ trafficking, with effects comparable to those of, or exceeding, the endogenous ligand. Nuclear translocation of ERβ is a pivotal step in the activation of "classical" signaling pathways, as the receptor must localize to the nucleus to bind specific DNA sequences and regulate the expression of target genes.[11] Thus, the enhanced nuclear localization of ERβ in response to OleA or HT exposure appears to be a critical mechanism by which these compounds, similar to 17b, may influence various physiological processes, including the regulation of gene expression associated with cell proliferation, differentiation, and apoptosis, the modulation of inflammatory pathways and oxidative stress responses, as well as the maintenance of endocrine homeostasis and reproductive function.

3.2. Modulation of the intracellular Ca^{2+} flux

Estrogens rapidly modulate Ca^{2+} dynamics through non-classical signaling pathways, regulating both Ca^{2+} influx and release from intracellular stores.[44,45] Consistent with this, our results show that OleA and HT reproduce key features of estrogen-mediated Ca^{2+} signaling. Confocal microscopy analysis revealed a significant increase in total intracellular Ca^{2+} levels in SH-SY5Y fixed cells after 30 min of treatment with OleA and HT (10 nM), comparable to that induced by 17b at the same concentration; at higher concentration (5 μM), this effect was further greater and remained significant after 1 h, particularly in HT-treated cells (Fig. 3A and B). This response appears to be ERβ-mediated, as indicated by the significant decrease in Fluo-3 AM signals (green fluorescence) following PHTPP pre-treatment (Fig. 3A and B). In addition, 17b, OleA, and HT primarily induced Ca^{2+} release from the endoplasmic reticulum *via* ryanodine receptors (RyRs), as shown by the marked inhibition of Ca^{2+} flux in the presence of ryanodine and the partial reduction observed with 2-APB, an IP_3 receptor inhibitor (Fig. 3C).

The increase in intracellular Ca^{2+} levels observed in treated cells was also influenced by the activation of NMDA and AMPA receptors, that are involved in synaptic plasticity, learning and memory processes.[46] Consistently, we found that the expression of both receptors increased similarly in cells treated with 17b, OleA and HT with a more pronounced effect at higher concentrations (Fig. 3D and E). Notably, the increases of Ca^{2+} flux were not observed when the cells were pre-treated with memantine, an NMDA receptor inhibitor, or with CNQX, an AMPA receptor antagonist (Fig. 3F). These findings indicate that OleA and HT closely mimic 17b in modulating Ca^{2+} homeostasis, promoting both intracellular Ca^{2+} release and receptor-mediated Ca^{2+} influx, thereby further reinforcing their estrogen-like activity in neuronal cells.

3.3. EVOO-derived phenolic compounds modulate estrogen-dependent pathways

ERβ has been shown to modulate IGF1R phosphorylation *via* non-classical signaling, influencing synaptic function and neuronal survival.[14,47] In line with this evidence, our data indicate that OleA, at both concentrations tested and HT at 5 μM, significantly increased phospho-IGF1R (pIGF1R) levels, in a manner comparable to the increase elicited by 17b (Fig. 4A), suggesting estrogen-like activation of IGF1R-dependent survival pathways. This effect was markedly reduced by IGF1R inhibitor, AG538 (Fig. 4B), indicating that IGF1R activation is a key downstream event in the response to these compounds.

To better understand the functional correlation between IGF1R and ERβ modulation we evaluated ERβ expression following IGF1R inhibition. Notably, AG538 markedly attenuated ERβ signal intensity (Fig. 4C and D), indicating that IGF1R activity contributes to the maintenance of ERβ signaling. This effect was particularly evident in HT-treated cells and at the lower concentration of OleA, conditions that also showed a greater reduction in pIGF1R levels compared to 17b (Fig. 4A and B). These findings support the existence of a bidirectional cross-talk between ERβ and IGF1R signaling pathways, consistent with previous reports describing ERβ-mediated modulation of IGF1R activity *via* non-classical mechanisms.[48]

The downstream impact of this signaling convergence was further explored by analyzing key intracellular pathways. Treatment with 17b (10 nM) and OleA (5 μM) significantly increased ERK phosphorylations, as indicated by pERK/ERK ratio, confirming activation of mitogen-activated protein kinase (MAPK) pathways (Fig. 4E and F). Furthermore, OleA, HT and 17b induced the inhibitory phosphorylation of glycogen synthase kinase 3 beta (GSK3β) at serine 9, as demon-

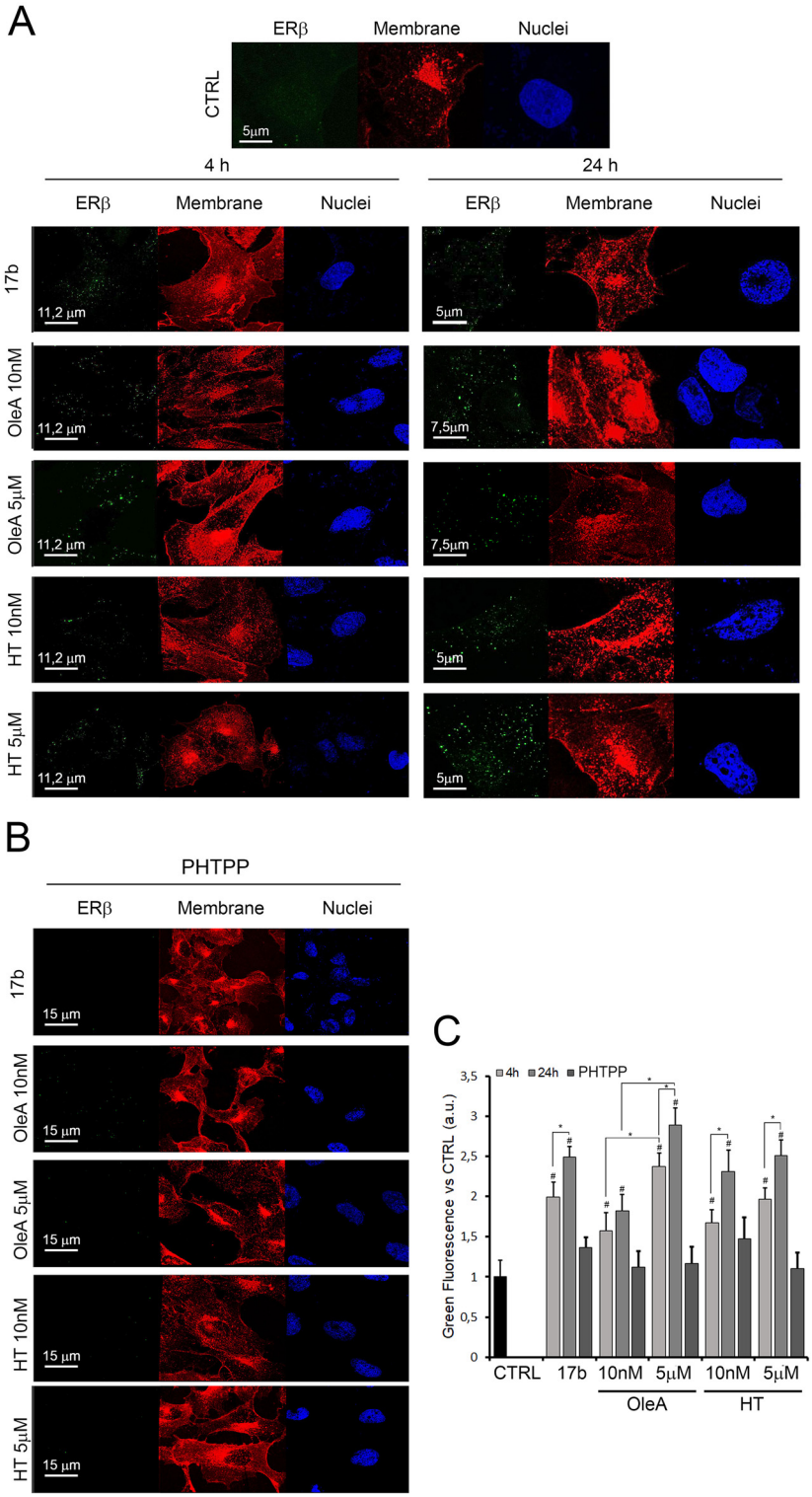

Fig. 1 17b, OleA and HT increase the overall expression of ERβ. SH-SY5Y cells were treated for 4 and 24 h with 10 nM 17b, OleA and HT at two different concentrations 10 nM and 5 μM. (A and B) Representative STED confocal images of three independent experiments of cells in absence (A) or in presence (B) of PHTPP, a selective ERβ full antagonist. Cell membranes were stained with tetramethylrhodamine-conjugated WGA (red fluorescence) and cell nuclei with Hoechst 33342 (blue fluorescence); ERβ was stained with anti-ERβ antibodies followed by treatment with Alexa 514-conjugated anti-rabbit secondary antibodies (green fluorescence). (C) Green fluorescence quantification performed by ImageJ software on 5 images from each experiment, 10 cells per image. Data are reported as the mean ± SE. Statistics: * $p < 0.05$; # $p < 0.05$ *vs.* CTRL. Scale bars were reported on images.

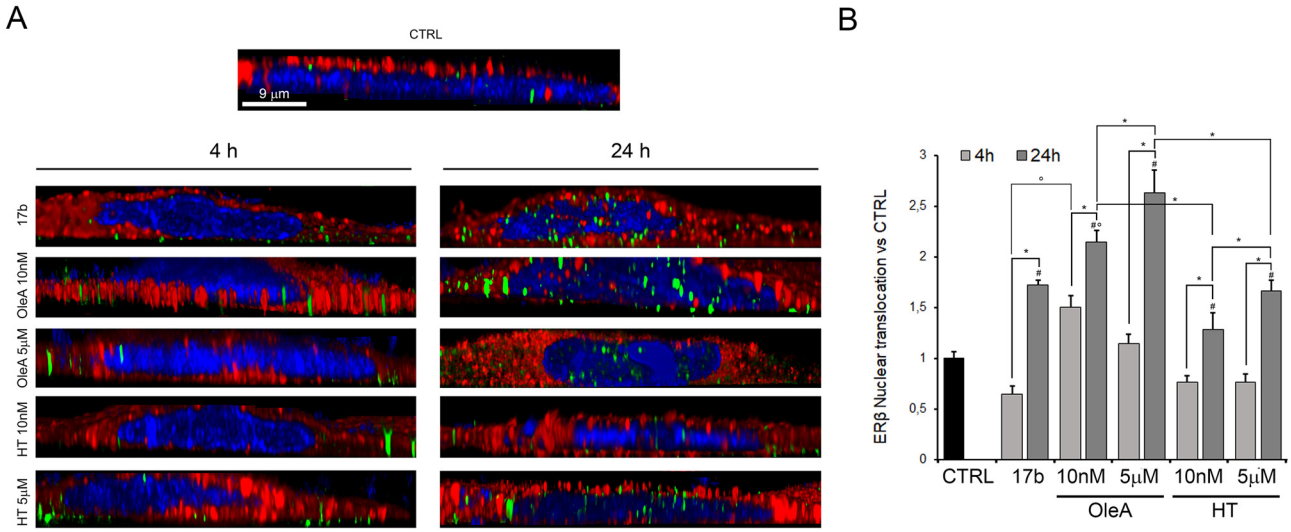

Fig. 2 17b, OleA and HT induce ERβ nuclear translocation. SH-SY5Y cells were treated for 4 and 24 h with 10 nM 17b, OleA and HT at two different concentrations 10 nM and 5 µM. (A) Representative 3D reconstruction of the *z*-stack analysis (4,2 µm-thick slices) of the specimens shown in Fig. 1. The cell was virtually dissected on the *zx* plane to show more clearly the nuclear localization of ERβ. Cell membranes were stained with tetramethylrhodamine-conjugated WGA (red fluorescence) and the nuclei with Hoechst 33342 (blue fluorescence); ERβ was stained with anti-ERβ antibodies followed by Alexa 514-conjugated anti-rabbit secondary antibodies (green fluorescence). The 9 µm scale bar reported on the CTRL is the same for all other images. (B) Quantification of intracellular translocation of ERβ performed by ImageJ software on 5 images from each experiment. Data are presented as mean ± SE. Statistics: * $p < 0.05$; # $p < 0.05$ *vs.* CTRL; ° $p < 0.05$ *vs.* 17b.

strated by a significant increase in pGSK3β/GSK3β ratio, particularly at 5 µM concentrations (Fig. 4E and G).

This dual mechanism of action on ERK and GSK3β underscores the intricate role of olive oil-derived phenolic compounds in regulating critical signaling pathways involved in cell survival and mitochondrial function. Notably, the inactivation of GSK3β has been associated with enhanced mitochondrial biogenesis, improved mitochondrial dynamics, reduced mitochondrial permeability, and decreased mitochondria-dependent apoptosis. Therefore, these findings suggest that EVOO-derived phenolic compounds may exert protective effects against mitochondrial dysfunction through the regulation of GSK3β activity.[49]

3.4. OleA and HT improve mitochondrial biogenesis

ERβ translocation to mitochondria is a key component of non-classical estrogen signaling, contributing to mitochondrial function and neuroprotection. In neuronal cells, mitochondrial ERβ has been associated with enhanced ATP production and improved mitochondrial membrane potential (MMP).[50,51] It has been reported that 17b promotes the relocalization of ERβ from the cytoplasm to mitochondria or mitochondria-associated regions through kinase-dependent signaling pathways, thereby influencing mitochondrial biogenesis and dynamics.[15,51] Given that OleA and HT modulate ERβ expression, we investigated whether these compounds could also affect mitochondrial localization of the receptor and, consequently, mitochondrial activity, biogenesis and MMP. Using a machine learning-based proximity analysis, we found that OleA significantly promoted ERβ translocation to mitochondrial regions even at low concentration (10 nM), with effects comparable to those observed with 17b (Fig. 5). Notably, this effect was significantly more pronounced than that induced by HT, which at the same concentration did not promote ERβ redistribution to mitochondria (Fig. 5B).

Once assessed that the OleA and HT increase ERβ expression, and that OleA promotes its translocation to mitochondrial proximity area, we moved on to analyze mitochondrial mass and membrane potential in SH-SY5Y cells treated for 4 and 24 h with 17b (10 nM), and with OleA or HT (10 nM and 5 µM) using the MitoTracker Red assay (Fig. 6A). Both 17b and OleA (5 µM) significantly increased mitochondrial number, showing an approximately three-fold rise compared to control conditions (Fig. 6A and B). OleA at 10 nM exerted a more modest effect, suggesting a dose-dependent response. Notably, HT showed the strongest effect with both concentrations significantly enhancing mitochondrial number, reaching approximately a two-fold increase at 10 nM and up to a four-fold increase at 5 µM (Fig. 6B). Despite the marked increase in mitochondrial number, no significant changes in MMP were observed as indicated by comparable fluorescence intensity per mitochondrion across treatments (Fig. 6C). This suggests that the increase in mitochondrial number is not accompanied by detectable alterations in mitochondrial functional status at the single-organelle level. To further investigate the underlying mechanisms, we evaluated the expression of peroxisome proliferator-activated receptor γ coactivator 1α, (PGC-1α), a key transcriptional coactivator in the regulation of mitochondrial biogenesis, oxidative capacity, and antioxidant defence mechanisms. Immunofluorescence analysis, (Fig. 6A and D) showed that OleA and HT increased PGC-1α expression only at 5 µM, in line with the effect of 17b and with the

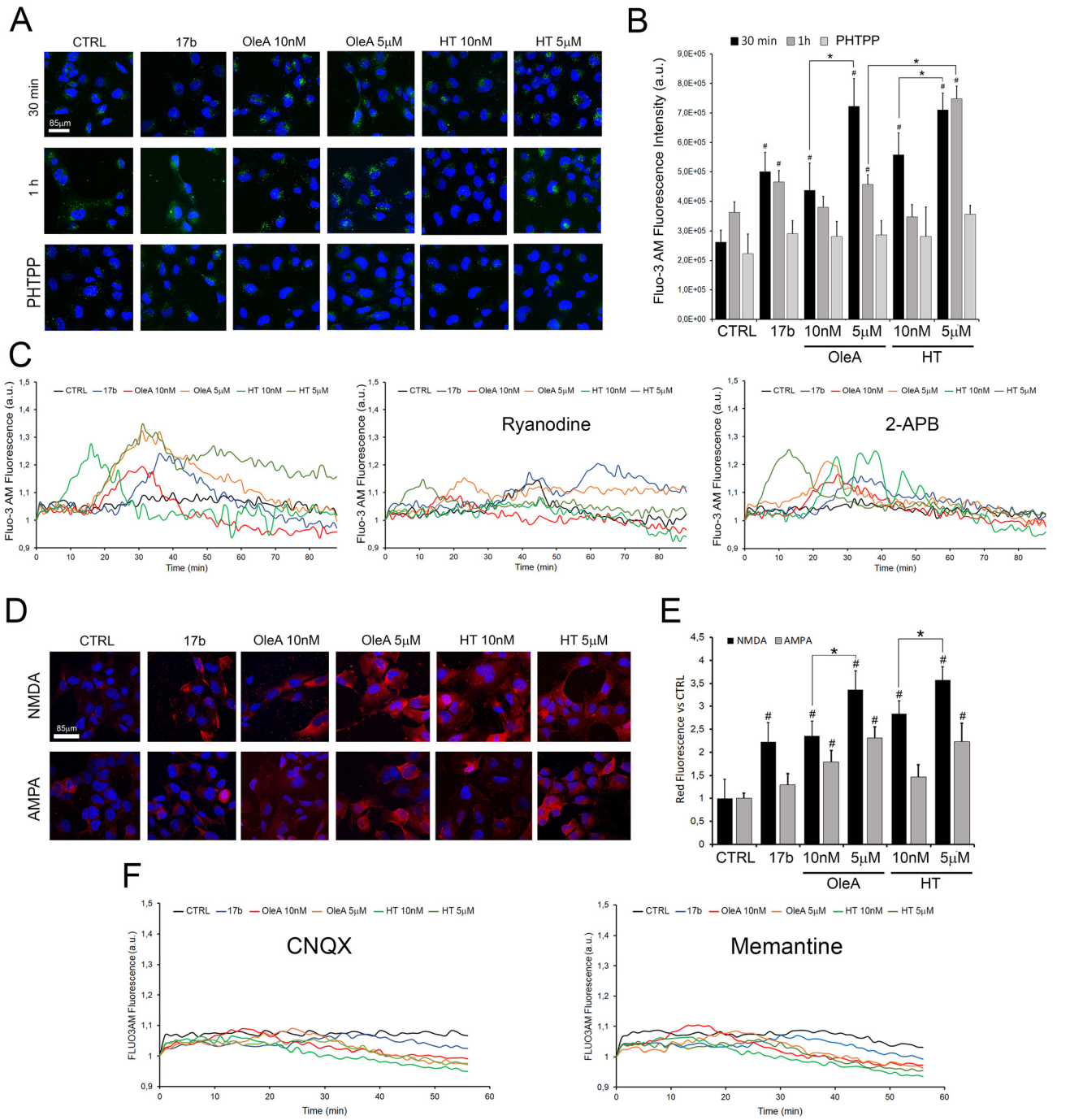

Fig. 3 17b, OleA and HT modulate Intracellular Ca^{2+} flux. SH-SY5Y cells were treated for 30 min and 1 h with 17b (10 nM), OleA (10 nM or 5 µM), and HT (10 nM or 5 µM), either without (−PHTPP) or with (+PHTPP) pre-treatment with PHTPP (100 nM, 30 min) together with the AMPA receptor antagonist CNQX (5 µM) or the NMDA receptor inhibitor memantine (10 µM). (A) Cells were loaded with Fluo-3 AM (green fluorescence) 15 min before treatment. After treatment, the nuclei were stained with Hoechst 33342 (blue fluorescence). (B) Quantification of green fluorescence intensity per cell was performed across approximately five different acquisitions. Data are reported as mean ± SE. Statistics: * $p < 0.05$; # $p < 0.05$ *vs.* CTRL. (C) Live-cell Ca^{2+} experiments measuring intracellular Ca^{2+} flux. SH-SY5Y cells were pre-treated with ryanodine (Rya 10 µM) and 2-APB (100 µM) for 1 h to block the RyR- and IP3 receptors-mediated Ca^{2+} release, respectively, and were loaded with Fluo-3 AM (green fluorescence) 15 min before treatment. Green fluorescence was continuously recorded for 85 min. (D) Representative confocal microscopy images of NMDA and AMPA receptors expression. Nuclei were stained with Hoechst 33342 (blue fluorescence) and receptors with primary antibodies against NMDA or AMPA receptors, followed by Alexa 568-conjugated anti-mouse secondary antibodies (red fluorescence). Scale bars: 85 µm. (E) Quantification of red fluorescence intensity per cell, corresponding to NMDA and AMPA receptor levels, from approximately 5 independent images. Data are reported as mean ± SE. Statistics: * $p < 0.05$; # $p < 0.05$ *vs.* CTRL. (F) Live-cell Ca^{2+} experiments measuring intracellular Ca^{2+} flux. SH-SY5Y cells were pre-treated with CNQX (5 µM) or with memantine (10 µM) for 1 h and loaded with Fluo-3 AM 15 min before treatment. Green fluorescence was continuously recorded for 55 min.

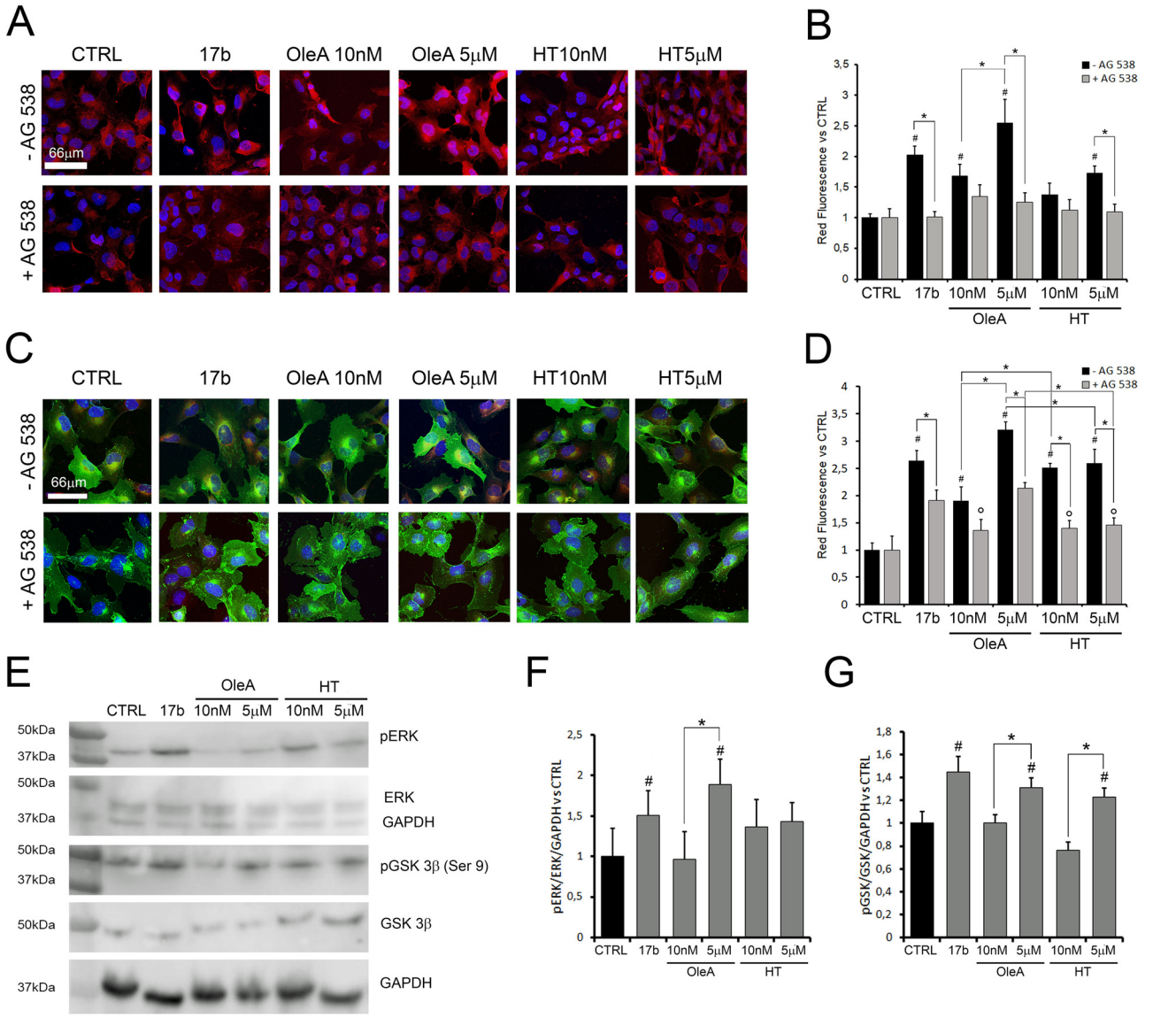

Fig. 4 Involvement of IGF1R and MAPK signaling pathways induced by 17b, OleA and HT. SH-SY5Y cells were treated for 24 h with 17b (10 nM), OleA or HT (10 nM and 5 μM). Where indicated, cells were pre-treated for 1 h with the IGF1R inhibitor AG538 (2 μM). (A) Representative confocal images of phospho-IGF1R (pIGF1R) in untreated cells (–AG538) and in AG538-pre-treated cells (+AG538). Cells nuclei were labelled with Hoechst 33442 (blue signal), and pIGF1R was detected using a specific primary antibody followed by Alexa Fluor 568-conjugated secondary antibodies (red). (B) Quantification of pIGF1R fluorescence intensity per cell from three independent experiments (about 15 cells for image). Data are presented as mean ± SE. Statistics: * $p < 0.05$; # $p < 0.05$ *vs.* CTRL. (C) Representative confocal images of ERβ expression in untreated (–AG538) and AG538-pre-treated (+AG538) cells. Nuclei were stained with Hoechst 33342 (blue), cell membranes with CTX-B Alexa Fluor 488 (green), and ERβ was detected using specific primary antibodies followed by Alexa Fluor 568-conjugated secondary antibodies (red). (D) Quantification of ERβ fluorescence intensity per cell from three independent experiments (about 15 cells for image). Data are presented as mean ± SE. Statistics: * $p < 0.05$; # $p < 0.05$ *vs.* CTRL; ° $p < 0.05$ *vs.* 17b. (E) Representative Western blots showing pERK, ERK, pGSK3β, GSK3β, and GAPDH protein levels. Full-length blots are reported in SI Fig. S1. Densitometric analysis of pERK/ERK (F) and pGSK3β/GSK3β (G) ratios was performed on at least three independent experiments, normalized to GAPDH and expressed relative to CTRL. Data are presented as mean ± SE. Statistics: * $p < 0.05$; # $p < 0.05$ *vs.* CTRL.

observed increase in mitochondrial number. In contrast, at 10 nM, 17b appears to be more effective than both OleA and HT at the same concentration.

Overall, these findings indicate that OleA and HT promote mitochondrial biogenesis, as supported by the increase in both mitochondrial number and PGC-1α expression. The absence of changes in MMP further suggests that this increase reflects an expansion of the mitochondrial network rather than alterations in mitochondrial functional integrity.

3.5. ABAD involvement in mitochondrial estrogenic metabolism induced by EVOO-derived phenolic compounds

Considering the well-established effects of estrogens on mitochondrial function, we also sought to evaluate the involvement

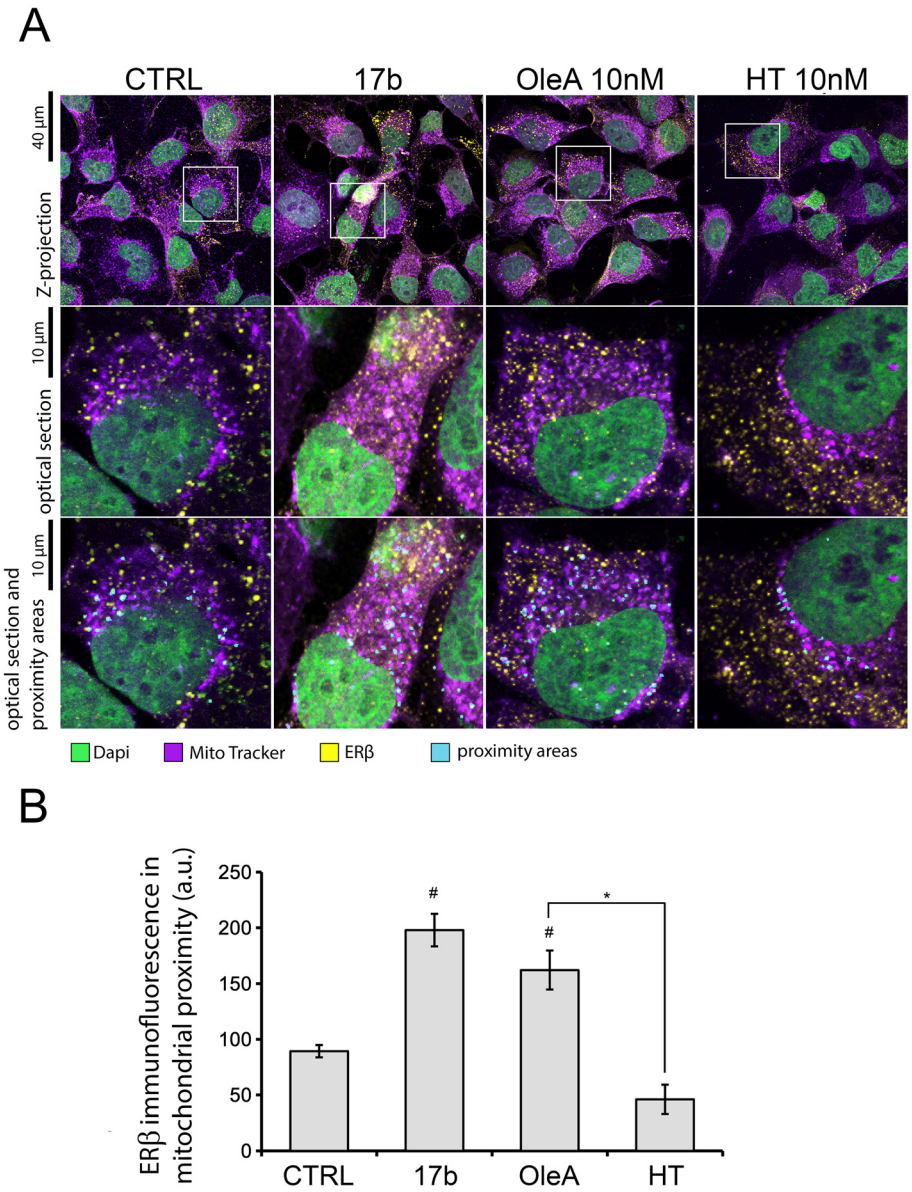

Fig. 5 17b and OleA promote ERβ localization in proximity to mitochondria. (A) SH-SY5Y cells were treated for 24 h with 17b (10 nM), OleA or HT (10 nM). Cells were then immunolabeled for ERβ (yellow). The mitochondria (magenta) and nuclei (green) were then revealed with MitoTracker Red and Hoechst 33342, respectively. The first row shows Z-stack projections of the three fluorescent signals. The second row displays representative single optical sections passing through cytoplasmic portions of the cells. The third row highlights regions of ERβ localization in proximity to mitochondria (cyan), identified by proximity analysis. (B) Quantification of ERβ–mitochondria proximity from three independent acquisitions (≈10 cells per image). Data are reported as mean ± SE. Statistics: * $p < 0.05$; # $p < 0.05$ *vs.* CTRL.

of ABAD, also known as 17b-hydroxysteroid dehydrogenase type 10 (17b-HSD10). ABAD physiologically converts 17b to estrone and plays a key role in estrogen metabolism.[52] Its expression levels are tightly linked to neuronal homeostasis as optimal 17b levels are critical for neuronal survival. Previous research has demonstrated that 17b can upregulate ABAD expression and modulate mitochondrial bioenergetics, although ABAD has also been implicated in Aβ-related neurodegeneration.[2]

In our cellular model, confocal microscopy images (Fig. 7A) demonstrated that 17b, OleA, and HT significantly increased ABAD expression after 24 hours of treatment. While 17b induced a moderate increase compared to control cells, OleA and HT elicited a more pronounced upregulation. Notably, HT, especially at 10 nM, exerted a significantly greater effect than 17b (Fig. 7B).

Western blot analysis (Fig. 7C and D) confirmed the overall upregulation of ABAD protein levels across all treatments, although the magnitude of the increase appeared less pronounced compared to that observed by confocal microscopy. While OleA and HT still showed higher ABAD levels relative to 17b, the differences between treatments were more moderate, suggesting that the stronger effect observed by imaging may

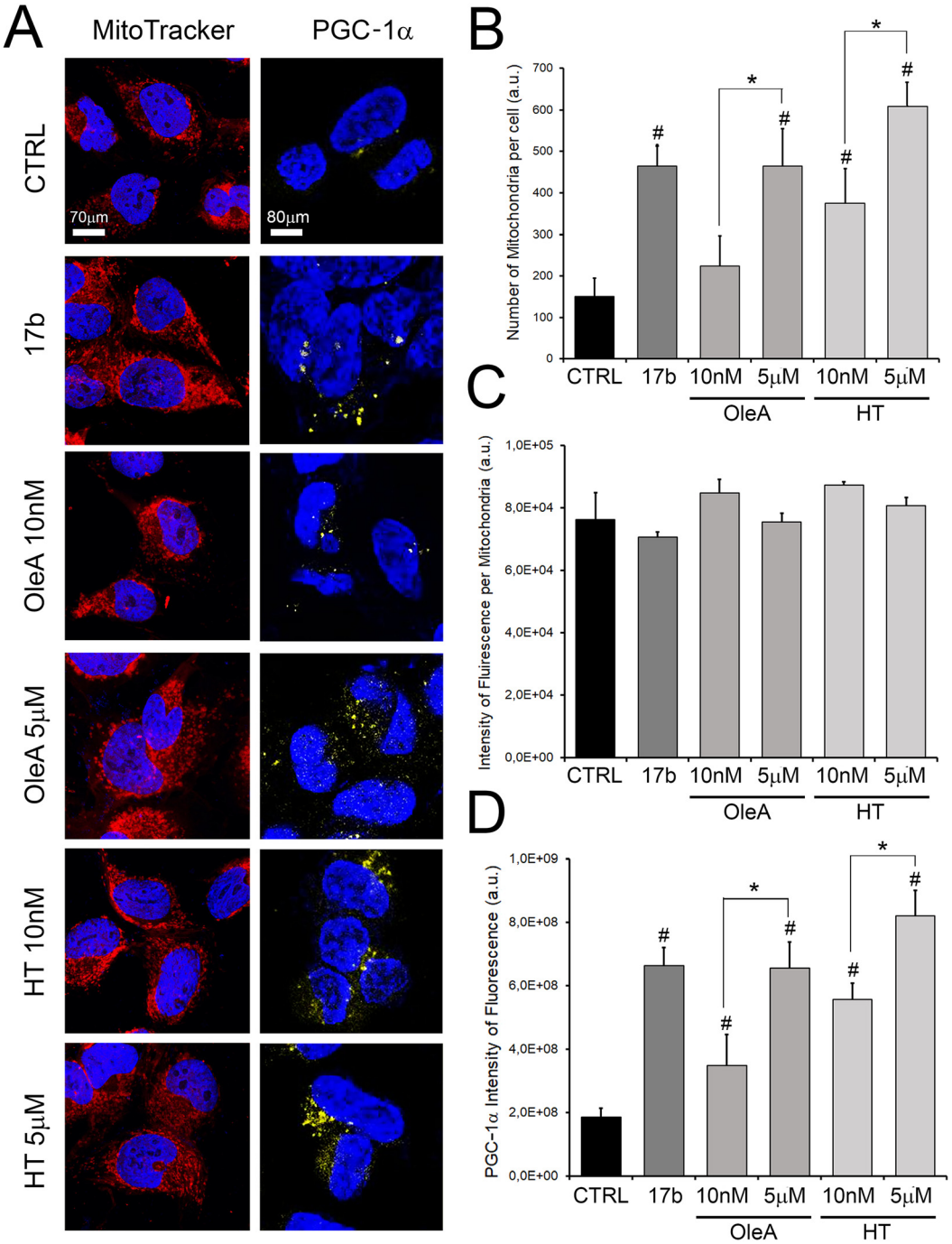

Fig. 6 17b, OleA and HT promote mitochondrial biogenesis in SH-SY5Y cells. SH-SY5Y cells were treated for 24 h with 10 nM 17b, OleA and HT at two concentrations, 10 nM and 5 μM. Cell nuclei were stained with Hoechst 33342 (blue fluorescence); mitochondria with MitoTracker Red probe; PGC-1α was stained with anti-PGC-1α antibodies followed by Alexa 568-conjugated anti-rabbit secondary antibodies. (A) Representative confocal images showing mitochondria (red), PGC-1α (yellow) and nuclei (blue). Quantitative analysis is reported in the corresponding histograms: (B) Mitochondria number, (C) MitoTracker Red fluorescence intensity and (D) PGC-1α signal, were quantified using ImageJ software on 5 images for condition, with 4 cells analysed per image. Data are presented as mean ± SE. Statistics: * $p < 0.05$; # $p < 0.05$ *vs.* CTRL.

reflect, at least in part, enhanced local concentration or redistribution of ABAD within mitochondria rather than a proportional increase in total protein abundance.

To our knowledge, this is the first report describing the modulation of ABAD expression by EVOO-derived phenolic compounds. Importantly, despite the increase in ABAD levels, neither OleA nor HT induced cytotoxic effects or mitochondrial dysfunction, as also supported by previous studies.[23–25] Taken together, these findings suggest that the upregulation of ABAD induced by OleA and HT is associated with enhanced

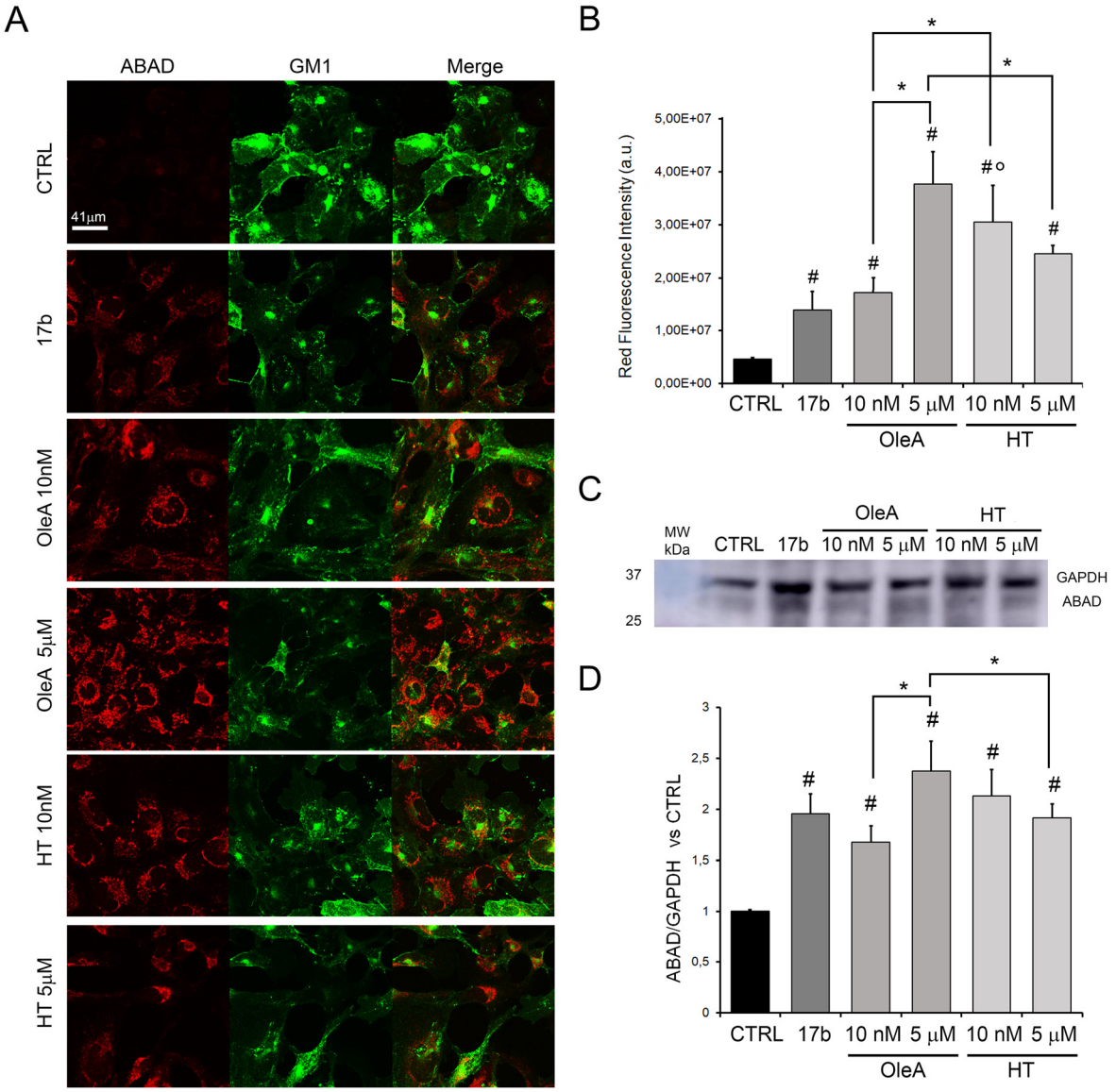

Fig. 7 Upregulation of mitochondrial enzyme ABAD expression. SH-SY5Y cells were treated for 24 h with 17b (10 nM), OleA, or HT (10 nM and 5 μM). (A) Representative confocal images showing ABAD expression. Cell membranes were labeled with CTX-B-488 (green signals) and ABAD was detected by using a specific primary antibody followed by Alexa Fluor 568-conjugated secondary antibodies (red signals). (B) Quantification of ABAD fluorescence intensity per cell from three independent acquisitions (about 10 cells per image). Data are reported as mean ± SE. Statistics: * $p < 0.05$; # $p < 0.05$ *vs.* CTRL; ° $p < 0.05$ *vs.* 17b. (C) Representative Western blots of ABAD expression normalized to GAPDH from at least three independent experiments. The images were cropped from the full gels reported in the SI Fig. 1S. (D) Quantification of signals was determined by densitometric analysis of at least three independent experiments, normalized to GAPDH signals. All blot signals were normalized to the CTRL. Error bars represent SE. Statistics: * $p < 0.05$; # $p < 0.05$ *vs.* CTRL.

mitochondrial remodeling rather than pro-neurodegenerative mechanisms, consistent with an estrogen-like mode of action.

3.6. A global overview of molecular changes associated with EVOO-derived phenolic compounds treatment in intact cells through untargeted FTIR microspectroscopy analysis

We applied FTIR microspectroscopy coupled with partial least square-discriminant analysis (PLS-DA) to explore the infrared absorption of intact SH-SY5Y cells exposed to 17b and compare it with that of OleA and HT. This label free vibrational technique makes it possible to hunt, in an untargeted way, for possible IR spectroscopic markers that outline the cellular effects of 17b, OleA and HT *in situ*.

In Fig. 8, the FTIR analysis of intact SH-SY5Y cells treated with 10 nM 17b, 10 nM or 5 μM OleA, and of the control untreated cells is displayed. In Fig. 8A we reported the mean second derivative spectra between 3050–2800 cm^{-1}, a spectral range dominated by the absorption of methyl (~2959 cm^{-1} and ~2872 cm^{-1}) and methylene (~2922 cm^{-1} and ~2852 cm^{-1}) groups mainly from lipid hydrocarbon chains.[53,54] As it can be

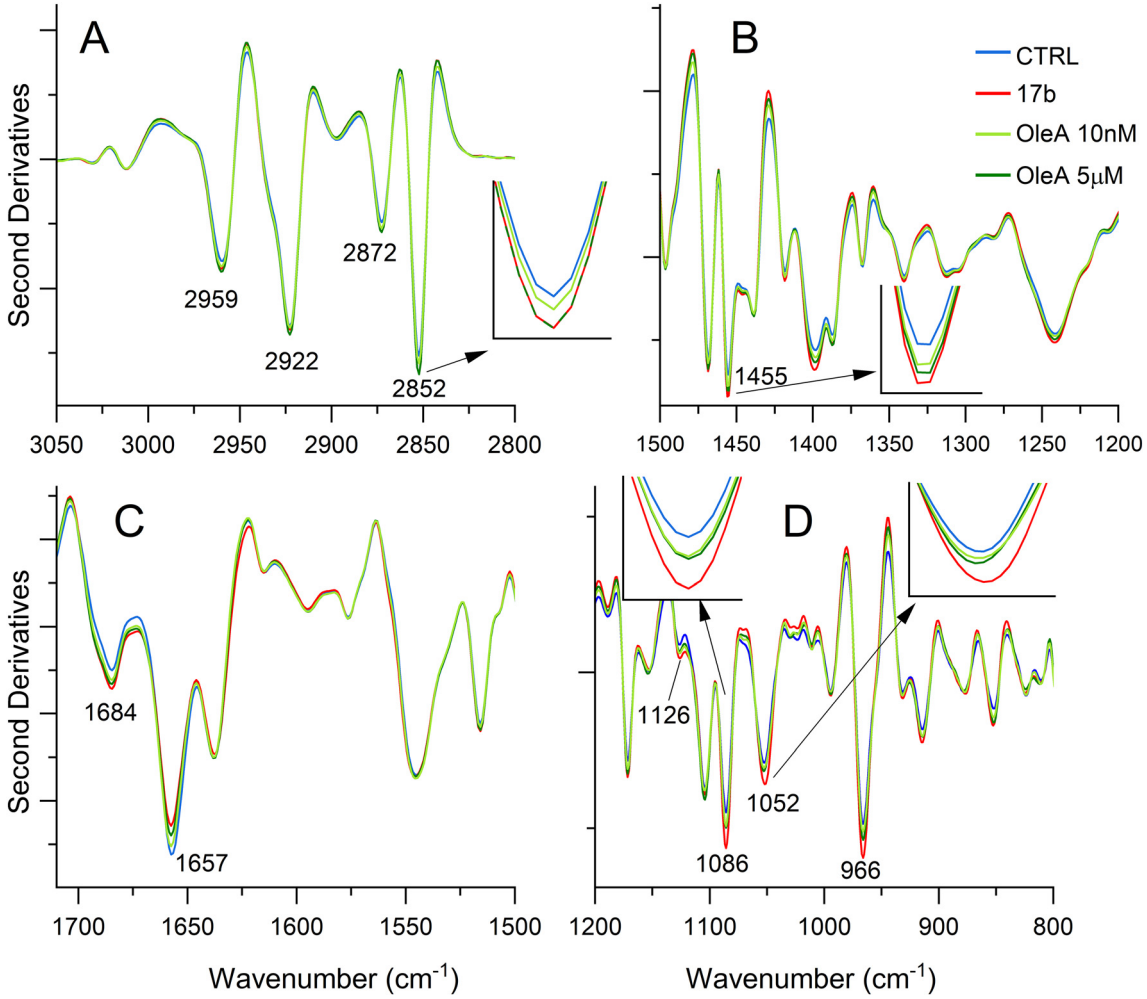

Fig. 8 FTIR analysis of SH-SY5Y cells treated with OleA. Mean second derivative spectra of intact SH-SY5Y cells treated with OleA in all the analyzed spectral ranges (A)–(D). For comparison, also the second derivatives of cells treated with 17b and CTRL are reported. The second derivatives are provided in the SI.

seen, treated cell spectra display a higher intensity of the CH_2 bands compared to control cells; in particular, the intensity variation of the ~2852 cm^{-1} component, due to CH_2 symmetric stretching, has been found significantly higher for cells treated with 17b and OleA 5 μM (Fig. 9A). From the analysis of the 1500–1200 cm^{-1} spectral range (Fig. 8B), due to the overlapping absorption of methyl and methylene groups from different biomolecules, including lipid hydrocarbon chains and head groups, and of phosphate groups mainly from nucleic acids and lipids, the ~1455 cm^{-1} band, due mainly to CH_3 deformation,[53,54] emerges as that carrying the higher spectral variance. Its intensity increase, compared to control cells, was found to be highly significant for all the treatments (Fig. 9B). Overall, these results point to a significant variation of the physico-chemical properties of cell lipids, in particular for cells exposed to 17b, as indicated by the classification accuracies reported in Fig. 9H.

Moreover, we analyzed the spectral range between 1700–1500 cm^{-1} (Fig. 8C), dominated by the Amide I and II bands, which provide information on possible modifications of the structural properties of the whole cell proteins. As it can be seen, the different treatments affect the band at ~1657 cm^{-1}, due to alpha-helices and/or random coils,[55] that decreases in intensity compared to control cells. Notably, PLS-DA identified the component band at ~1684 cm^{-1}, mainly assigned to β-sheets and/or turns,[55,56] as relevant for the discrimination between each treatment and untreated cells (see Fig. 9C). Overall, the spectral variations observed in the Amide region were significant for the treatment with 17b (discrimination accuracy of 0.82) and for 5 μM OleA (discrimination accuracy of 0.72) (Fig. 9H). We then moved to the fingerprint region, below 1200 cm^{-1} (Fig. 8D), where complex carbohydrate moieties and phosphate vibrations mostly occur. A combination of multivariate and univariate analyses has been necessary to identify the spectral components most relevant for the discrimination between treated and untreated cells. Two components have been pulled out: at ~1052 cm^{-1}, due to C–O vibrations of carbohydrates with also contributions from

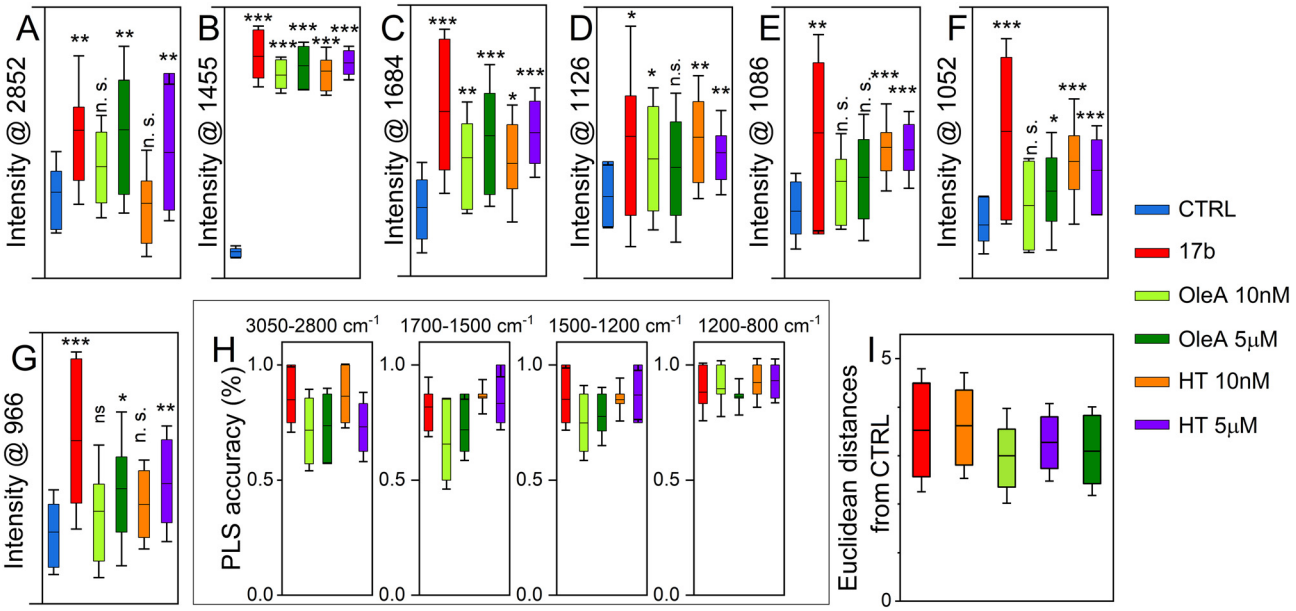

Fig. 9 Uni- and multivariate analyses of FTIR spectra: identification of spectroscopic markers of SH-SY5Y cell response to treatments. (A–G) Peak intensity of selected spectral components, identified by PLS-DA, for all the studied treatments compared to control samples. The intensities were taken from inverted second derivatives, provided in the SI. Statistical significance was determined using a two-sample *t*-test for comparisons with CTRL and is indicated as: n.s., $p > 0.05$; * $p < 0.05$; ** $p < 0.01$; *** $p < 0.001$. (H) PLS-DA accuracies for each of the analyzed spectral ranges. (I) Box plots representing the distribution of distances among spectra for each treatment, distances have been computed between the CTRL and the treated cells. Distances significantly differ from 0 (p-value $\ll 1 \times 10^{-16}$) in all cases based on *t*-test with multiple comparison correction (Bonferroni, see Table S1 for details). Statistical significance of the differences among the treatments was computed using one-way ANOVA followed by pairwise comparisons with Tukey's multiple comparison correction (see Table S2 for details). In A–I, each box is determined by the 25th and 75th percentiles, the black horizontal line within the box is the mean, and whiskers represent the standard deviations.

lipids,[54,56] and at ~966 cm^{-1} mainly due to the asymmetric stretching of $N(CH_3)_3$, from phosphatidylcholine (PC) and/or sphingomyelin (SM),[53,54] with also contribution from DNA backbone and ribose phosphate main chain vibrations 57. Considering the simultaneous increase in intensity of the above bands upon treatment with 5 μM OleA and 17b (Fig. 9E and F), we tentatively assign them mainly to lipids, particularly PC and/or SM. Indeed, to support this data, also the band at ~1400 cm^{-1}, due to the symmetric bending of $N(CH_3)_3$, displays the same spectral behaviour upon OleA treatment (Fig. 8B). Overall, this result points to a variation of the cell lipidome induced in particular by the treatment with 5 μM OleA and 17b. In addition to the above bands, the component at ~1126 cm^{-1} – mainly ascribable to lactate[58] also emerges as relevant for the PLS-DA accuracy (see Fig. 9H).

In general, the discrimination accuracy between control and treated cells resulted in excellent results for all three molecules, as reported in Fig. 9H.

Analogously to OleA treatments, we also investigated the IR absorption of cells treated with HT, and we again compared its response with that of untreated cells and cells treated with 17b (Fig. 10). In the spectral range between 3050–2800 cm^{-1}, an overall slight increase of the intensity of the CH_2 and CH_3 groups was observed for all the analyzed treatments compared to control cells. Moreover, the CH_3 absorption at ~1455 cm^{-1} increases significantly in intensity upon HT treatment (Fig. 9C), leading to an excellent discrimination, comparable to that found for 17b (Fig. 9H). Therefore, also HT treatment at the two concentrations induces important modifications of the physico-chemical properties of cell lipids.

Moreover, in the Amide band range (Fig. 10C), 10 nM HT treated cell spectrum displays a decreased intensity of alpha helix/random coil absorption at 1657 cm^{-1}, compared to control cells. However, as seen for OleA and 17b treatments, HT perturbs mainly the component at ~1684 cm^{-1}, due to β-sheet and/or turn structures that increase in intensity compared to control cells. Notably, the overall discrimination accuracies in this spectral range were found to be higher than 0.8 for both HT concentrations (Fig. 9H).

Furthermore, in the fingerprint region (Fig. 10D) three components have been pulled out as carrying the higher spectral variance between treated and untreated cells: ~1086 cm^{-1}, ~1052 cm^{-1}, ~966 cm^{-1}. In addition to those already discussed for OleA (~1052 cm^{-1} and ~966 cm^{-1}), the ~1086 cm^{-1} band is due to the overlapping absorption of phosphates (symmetric (PO_2^-) stretching mode) from nucleic acids and phospholipids, and of carbohydrates (stretching of (C–O) and (C–C), bending of (COH)).[53,56,57] Taking into consideration the simultaneous intensity increases of the above bands (Fig. 9E–G and 10D), we speculate that they might be mainly assigned to lipid moieties. Finally, we should mention the ~878 cm^{-1} and ~824 cm^{-1} bands that emerge as relevant for the discrimi-

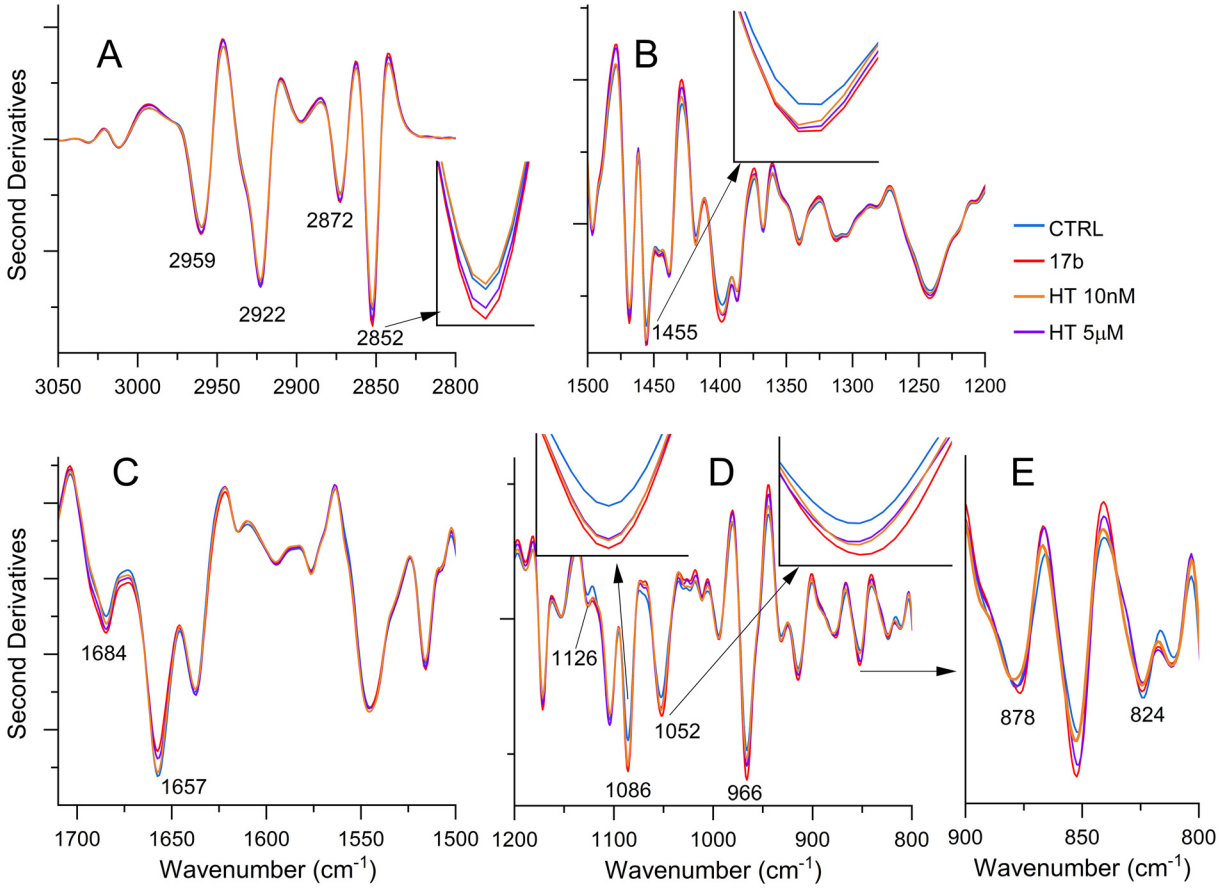

Fig. 10 FTIR analysis of SH-SY5Y cells treated with HT. Mean second derivative spectra of intact SH-SY5Y cells treated with HT in all the analyzed spectral ranges (A)–(E). For comparison, also the second derivatives of cells treated with 17b and CTRL are reported. The second derivatives are provided in the SI.

nation between HT and untreated cells (see inset of Fig. 10E). The ~878 cm^{-1} component is ascribable to vibrations from aldopyranose compounds[59] and from lipids, particularly C–N bonds of the quaternary ammonium group typical of cholines.[60] Furthermore, the ~824 cm^{-1} absorption is mainly assigned to carbohydrate C1–H rings involved in glycosidic linkage.[61] Interestingly, these two bands were found to change in shape rather than in intensity, supporting a modification of lipid and of carbohydrate physico-chemical properties induced by the exposure to HT.

Finally, taking into account the overall spectral components with the highest spectral variance, we calculated the relative spectral distances between untreated and treated cells for each molecule (Fig. 9I). Notably, 17b and HT 10 nM resulted in a higher level of activity on SH-SY5Y cells, compared to the other treatments.

3.7. Energy metabolism evaluation

Given the results obtained by FTIR microspectroscopy that showed variation in lactate content in SH-SY5Y treated with 17b and HT, we have decided to investigate glycolysis through the Seahorse Glycolysis Stress Test (Fig. 11A and B). 17b and 5 μM OleA treated cells behave like control cells, having comparable ECAR profile as well as glycolysis and glycolytic capacity, while treatment with 5 μM HT enhanced only glycolytic capacity without changing basal glycolysis. On the contrary, cells treated with OleA and HT at a final concentration of 10 nM possessed the more enhanced glycolytic basal level and capacity, which results significantly higher for OleA-treated cells than the 17b and 5 μM OleA groups. Finally, HT treated cells and cells treated with 10 nM OleA had the higher glycolytic reserve, which is a measure of cells capability to respond with glycolysis to an energetic demand (Fig. 11B). Since the administration of these molecules seems to affect the glycolytic metabolism, we have decided to measure not only the amount of ATP produced through glycolysis, but also its total amount and the quantity derived from oxidative phosphorylation. Interestingly, the Seahorse ATP Rate Assay in Fig. 11C showed no significant difference in glycolytic ATP production. However, it is possible to observe how cells exposed to 10 nM HT significantly increased their mitochondrial ATP production compared to both control cells and 17b treated cells, and total ATP amount, with respect to 17b treated cells. Finally, the energetic phenotype was investigated by using the Seahorse Cell

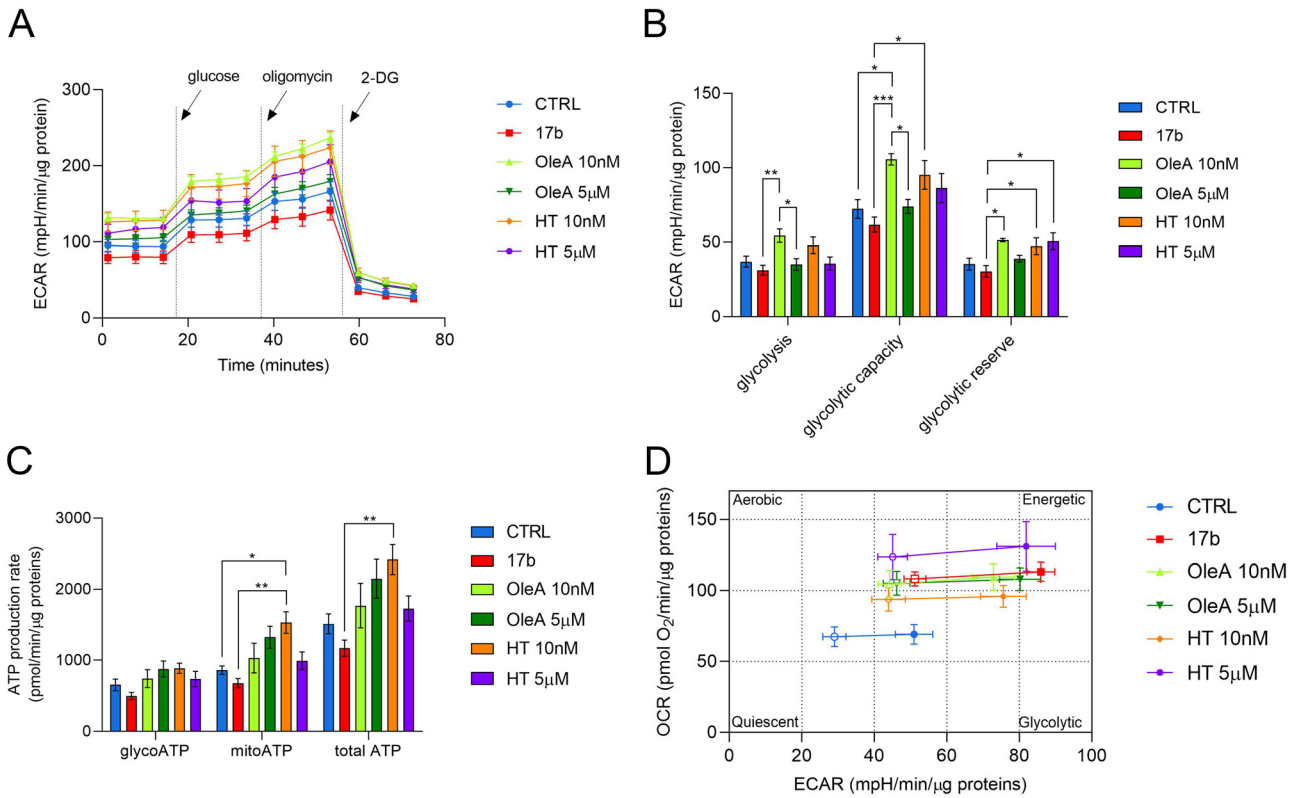

Fig. 11 Seahorse analysis of SH-SY5Y control and treated cells. (A) Representative ECAR profile expressed as mpH min^{-1} μg^{-1} proteins of Agilent Seahorse XF Glycolysis Stress Test. The arrows indicate the time of addition of 10 mM glucose, 1 μM oligomycin and 50 mM 2-deoxy-D-glucose (2-DG). (B) Analysis of basal glycolysis, glycolytic capacity and glycolytic reserve through Agilent Seahorse XF Glycolysis Stress Test. Bars indicate the mean ± SEM of three biological replicates. (C) Glycolytic, mitochondrial and total ATP production rate measured with the Agilent Seahorse XF ATP Rate Assay Kit by adding 1.5 μM oligomycin followed by 1 μM rotenone and antimycin A. Bars indicate the mean ± SEM of three biological replicates. (D) Energetic panel (*xy* graph) of control and treated cells obtained by Agilent Seahorse XF Cell Energy Phenotype Test by simultaneous addition of 1 μM oligomycin and 2 μM FCCP. Open symbols represent baseline conditions and closed symbols the stressed ones. One-way ANOVA with Tukey's correction was used to evaluate statistical significance within the different samples. Statistically significant: *$p < 0.05$, **$p < 0.01$ and ***$p < 0.001$.

Energy Phenotype Test (Fig. 11D). The xy graphs showed cells ability to meet an energy demand by upregulating glycolysis, independently from the compounds administered, and a more energetic and glycolytic profile of all treated groups compared to control cells at both basal and stressed conditions. Moreover, while the energetic phenotypes of 17b and OleA cells were quite similar, the energy profile of HT treated cells exhibited a dose-dependency with 5 μM HT being most effective in increasing the energetic metabolic profile.

4. Discussion

In the present study, we investigated the molecular effects of OleA and HT, two major EVOO-derived phenolic compounds, on estrogen-related signaling, Ca^{2+} homeostasis, mitochondrial remodeling, lipid composition, and energy metabolism in SH-SY5Y neuronal cells. Our findings demonstrate that these compounds reproduce key features of estradiol-mediated signaling, supporting their classification as estrogen-like modulators in a neuronal context.

The concentrations used in this study should be interpreted as mechanistic reference ranges rather than direct equivalents of dietary brain exposure. HT is systemically absorbed mainly as conjugated metabolites, while the brain availability of OleA in its intact form remains poorly defined. Nevertheless, the responses observed here provide useful mechanistic insight into signaling pathways that may be influenced by repeated exposure to olive-derived phenolics or by their circulating metabolites.

A central finding of this work is that OleA and HT promote ERβ nuclear translocation and activate MAPK/ERK signaling, pathways implicated in neuronal survival, proliferation, and stress resilience. These observations are consistent with membrane-initiated estrogen signaling mechanisms that sustain neuronal metabolic competence.[9] The engagement of the ERβ–IGF-1R axis further supports the concept of cross-talk between estrogen receptors and growth factor pathways, which cooperate in neuronal survival and metabolic regulation.[62,63] Estrogen receptors are functionally interconnected with IGF-1R-dependent PI3K/Akt and MAPK/ERK cascades, which converge on mitochondrial regulation and cellular bioener-

getics. The ERβ/IGF-1R/ERK dependency observed in our model therefore suggests that OleA and HT act through integrated signaling networks rather than as classical high-affinity receptor ligands. Such a mechanism is consistent with the broader behavior of dietary bioactives in neuronal systems. Several polyphenols intersect estrogen-related signaling while simultaneously modulating mitochondrial and metabolic pathways. For example, resveratrol and quercetin activate ER-dependent mechanisms and promote mitochondrial biogenesis through SIRT1/PGC1α signaling,[64,65] whereas genistein acts as a preferential ERβ agonist and influences MAPK/ERK cascades in neural models.[66] Similarly, other nutraceutical molecules with documented brain exposure modulate insulin/IGF-related signaling hubs that interface with estrogen pathways. Nuciferine, an aporphine alkaloid capable of crossing the blood–brain barrier, improves cognitive impairment in metabolically challenged models and engages insulin receptor/PI3K–AKT signaling.[67] Importantly, current evidence suggests that such compounds primarily modulate insulin/IGF pathway activity rather than acting as direct receptor ligands.[68] Taken together, these findings reinforce the view that dietary bioactive molecules regulate interconnected signaling networks rather than acting through single-target mechanisms.

The modulation of intracellular Ca^{2+} dynamics further supports the estrogen-like behaviour of OleA and HT. Both compounds increased intracellular Ca^{2+} levels through coordinated activation of NMDA and AMPA receptors, as well as Ca^{2+} release from intracellular stores.[69,70] This pattern closely resembles rapid estrogen signaling, in which Ca^{2+} fluxes cooperate with ERK activation to regulate transcriptional and neurotrophic responses.[71] Although BDNF and CREB phosphorylation were not directly assessed in the present study, the simultaneous activation of ERβ, ERK, and Ca^{2+} signaling observed here suggests the engagement of CREB-dependent transcriptional pathways, which are known to regulate neurotrophic factors such as BDNF and to support neuronal plasticity and survival. Future investigations should evaluate these downstream targets to further clarify the impact of OleA and HT on neuronal plasticity.

Mitochondrial remodeling emerged as another major target of OleA and HT. OleA promoted ERβ localization in proximity to mitochondria, suggesting modulation of mitochondria-associated estrogen signaling. Both OleA and HT induced mitochondrial biogenesis, as indicated by increased mitochondrial mass and upregulation of PGC-1α. The absence of changes in mitochondrial membrane potential suggests that this response reflects an expansion of the mitochondrial network rather than acute functional activation. The increase in PGC-1α is particularly relevant, as this coactivator orchestrates mitochondrial biogenesis, oxidative metabolism, and antioxidant defenses. Mitochondrial biogenesis is classically regulated by the PGC-1α–NRF1/NRF2–TFAM axis, in which TFAM controls mitochondrial DNA replication and transcription; recent evidence indicates that EVOO-derived compounds may act on this axis.[72] Although downstream mediators such as NRF1, NRF2, and TFAM were not directly assessed, the coordinated increase in PGC1α expression and mitochondrial mass is consistent with the involvement of this canonical regulatory axis. This adaptive response may enhance neuronal metabolic flexibility by increasing mitochondrial reserve capacity without altering membrane potential. Overall, our findings support the view that EVOO-derived phenolic compounds modulate mitochondrial architecture and function through ER-associated signaling networks.

The modulation of ABAD expression provides an additional link between OleA and HT treatment and mitochondrial energy metabolism. Elevated ABAD levels have been associated with improved mitochondrial bioenergetics and neuroprotection in transgenic models, where increased ABAD expression reduced stroke volume and neurological deficits.[73] Furthermore, ABAD has been associated with increased brain ATP levels and improved utilization of β-hydroxybutyrate as an alternative metabolic fuel under conditions of metabolic stress.[73] Through the regulation of mitochondrial proteins such as ABAD, EVOO-derived phenolic compounds may therefore contribute to maintaining neuronal energy homeostasis and protecting neurons from metabolic and oxidative stress associated with aging.

Seahorse metabolic profiling revealed a nuanced and concentration-dependent bioenergetic response. While 17b and higher concentrations of OleA produced relatively modest metabolic changes, low-dose OleA and HT enhanced glycolytic capacity and mitochondrial ATP production, indicating metabolic reprogramming rather than simple estradiol mimicry. The increase in glycolysis observed with 10 nM OleA was corroborated by increased lactate production detected by FTIR microspectroscopy, suggesting enhanced glycolytic flux not fully matched by mitochondrial respiration. In contrast, HT preferentially enhanced mitochondrial ATP production, indicating a shift toward oxidative metabolism. Such dose-dependent metabolic rewiring has been described for other polyphenols. Quercetin exhibits biphasic effects on mitochondrial respiration,[74] whereas resveratrol generally promotes oxidative phosphorylation through mitochondrial regulatory networks.[75] These observations suggest that OleA and HT promote metabolic flexibility, enabling neuronal cells to dynamically adjust the balance between glycolysis and oxidative phosphorylation according to cellular energetic demand.

Recent evidence further supports a direct mitochondrial mechanism for oleuropein derivatives. Gherardi *et al.* demonstrated that oleuropein binds to MICU1, a regulatory subunit of the mitochondrial calcium uniporter (MCU) complex, thereby enhancing mitochondrial Ca^{2+} uptake and stimulating Ca^{2+}-dependent metabolic enzymes such as pyruvate dehydrogenase.[76] The simultaneous activation of mitochondrial biogenesis and mitochondrial Ca^{2+} uptake may therefore optimize Ca^{2+}-mediated metabolic fluxes and ATP production, processes that typically decline with aging.

Mitochondrial function is also closely linked to the lipid composition of cellular membranes. FTIR analysis revealed that OleA and HT, similarly to 17b, modulate lipid-associated spectral signatures in SH-SY5Y cells. Increased intensity of

CH_2 (~2852 cm^{-1}) and CH_3 (~1455 cm^{-1}) vibrational bands, together with enhanced choline-associated signals, suggest changes in lipid content and membrane fluidity. Additional spectral features, including those associated with phosphatidylcholine and sphingomyelin in the fingerprint region, further indicate remodeling of membrane lipid composition. Such changes may influence membrane microdomains involved in receptor localization and signal transduction, including ERβ-mediated pathways and may facilitate membrane–protein interactions necessary for efficient electron transport chain activity and mitochondrial bioenergetics.

Although OleA and HT share common estrogen-like properties, their mechanisms of action are not identical. OleA appears to preferentially affect structural and receptor-associated processes, including ERβ localization and mitochondrial remodeling, whereas HT exerts a stronger influence on cellular bioenergetics, particularly ATP production and metabolic activity. In this context, both compounds engage IGF-1R signaling, albeit with a different degree of dependency, suggesting that this pathway serves as a shared regulatory hub rather than a uniformly activated target.

Collectively, the integration of ERβ activation, calcium signaling, mitochondrial biogenesis, lipid remodeling, and metabolic reprogramming indicates that OleA and HT coordinate multiple adaptive responses in neuronal cells. Rather than acting as simple estradiol mimetics, EVOO-derived phenolic compounds appear to function as integrative modulators of interconnected signaling and bioenergetic networks. From a nutritional perspective, these findings suggest that chronic exposure to EVOO phenolics, as occurs in Mediterranean dietary patterns, may contribute to maintaining neuronal metabolic adaptability even in the absence of overt pathological stress. By promoting coordinated adaptive responses rather than isolated pathway activation, OleA and HT may support cellular resilience mechanisms relevant to healthy brain aging and diet-associated neuroprotection.

5. Conclusion

The present study demonstrates that the EVOO-derived phenolic compounds, OleA and HT, engage coordinated estrogen-related signaling pathways in neuronal cells. By promoting ERβ activation and nuclear translocation, modulating IGF-1R/ERK signaling, regulating intracellular Ca^{2+} dynamics, and stimulating mitochondrial biogenesis and metabolic remodeling, these compounds act as integrative regulators of neuronal bioenergetic resilience. Rather than functioning as simple estradiol mimetics, OleA and HT appear to orchestrate crosstalk between hormonal and growth-factor signaling networks, linking receptor activation to mitochondrial adaptation, lipid remodeling, and metabolic flexibility. This multi-targeted mode of action aligns with emerging concepts of nutritional hormesis and network pharmacology, whereby sustained low-level exposure to dietary bioactives supports cellular adaptability and stress resistance. Although the concentrations employed *in vitro* cannot be directly equated with dietary brain exposure, the long-standing consumption of Olea europaea–derived products within Mediterranean dietary patterns, together with the documented systemic absorption of HT and related metabolites, supports the biological plausibility of cumulative neurometabolic effects. Overall, our findings provide mechanistic evidence that OleA and HT may contribute to the maintenance of neuronal energy homeostasis and resilience, supporting their potential relevance in nutritional strategies aimed at promoting healthy brain aging.

6. Limitations of the study

Several limitations should be acknowledged. First, the concentrations used *in vitro* (10 nM and 5 μM) were selected to explore dose-dependent pathway activation and to compare the effect of OleA and HT with those of 17b under controlled experimental conditions. These concentrations should be interpreted as mechanistic reference ranges rather than as direct reflections of levels achievable in human brain tissue following dietary intake. HT is systemically absorbed, primarily as conjugated metabolites, but its free concentration in the CNS after nutritional exposure remains incompletely defined. Similarly, the brain bioavailability of OleA and its derivatives requires further clarification.

Second, SH-SY5Y neuroblastoma cells, while widely used as a neuronal model, do not fully reproduce the complexity of mature neuronal networks, glial interactions, or the multifactorial processes underlying brain aging and neurodegeneration. Validation in differentiated neuronal models, primary neuronal cultures, co-culture systems, or organotypic systems will be essential to confirm the physiological relevance of these findings.

Third, although our data support activation of ERβ-linked neurotrophic, mitochondrial and metabolic pathways, several downstream effectors such as CREB/BDNF signaling, the NRF1/NRF2–TFAM mitochondrial biogenesis axis, mitochondrial respiration under stress conditions, and long-term neuroprotective outcomes should be evaluated in future studies.

Finally, the present study focused on acute or short-term cellular responses. Future investigations should determine whether sustained exposure to OleA, HT, or their metabolites produces durable protective effects under oxidative, metabolic, or neurodegenerative stress conditions. Addressing these points will be crucial to bridge the gap between mechanistic cellular findings and translational applications in nutritional neuroscience.

Author contributions

Conceptualization, M. L. and M. B.; investigation, formal analysis, methodology and validation M. L., D. N., F. C.; seahorse

experiments and data analysis: F. B., M. F., P. F.; FTIR experiments and data analysis: D. A., A. N.; multivariate analysis: P. M.; resources, M. B., P. F.; writing – original draft M. L., M. B., D. A., F. B., P. F.; writing – review and editing A. N., N. T., M. S., M. B.; funding acquisition, M. B.; supervision, M. B.

Conflicts of interest

The authors declare that they have no known competing financial interests or personal relationships that could have appeared to influence the work reported in this paper.

Abbreviations

17b	17b-Estradiol
2-APB	2-Aminoethyl diphenylborinate
ABAD	Amyloid-binding alcohol dehydrogenase
AD	Alzheimer's disease
AG 538	α-Cyano-(3-methoxy-4-hydroxy-5-iodocinnamoyl)-(3′,4′-dihydroxyphenyl) ketone, I-OMe-AG 538
AMPA	α-Amino-3-hydroxy-5-methyl-4-isoxazole propionic acid receptor
BDNF	Brain-derived neurotrophic factor
BBB	Blood-brain barrier
CaMKII	Ca^{2+}/calmodulin-dependent protein kinase II
CNQX	6-Cyano-7-nitroquinoxaline-2,3-dione
CREB	cAMP response element-binding protein
CTRL	Untreated cells
EREs	Estrogen response elements
ERβ	Estrogen receptor β
EVOO	Extra virgin olive oil
GSK3β	Glycogen synthase kinase 3 beta
HRT	Hormone replacement therapy
HT	Hydroxythyrosol
IGF1R	Insulin-like growth factor 1 receptor
IP3	1,4,5-Trisphosphate receptor
LDA	Linear discriminant analysis
LTP	Long-term potentiation
MAPK	Mitogen-activated protein kinase
Memantine	3,5-Dimethyl-1-adamantanamine hydrochloride
MMP	Mitochondrial membrane potential
NF-κB	Nuclear factor kappa-light-chain-enhancer of activated B cells
NMDA	N-Methyl-D-aspartate receptor
NRF1/NRF2	Nuclear respiratory factor 1 and 2
OleA	Oleuropein aglycone
PD	Parkinson's disease
PGC-1α	Peroxisome proliferator-activated receptor γ coactivator 1α
PHTPP	2-Phenyl-3-(4-hydroxyphenyl)-5,7-bis(trifluoromethyl)-pyrazolo[1,5-*a*]pyrimidine,4-[2-phenyl-5,7-bis(trifluoromethyl)pyrazolo[1,5-*a*]-pyrimidin-3-yl]phenol
Rya	Ryanodine
SE	Standard error
STED	Stimulated Emission Depletion (STED) super-resolution confocal microscopy
TMR	Tetramethylrhodamine
TSECs	Tissue-selective estrogen complexes
TFAM	Mitochondrial transcription factor A

Data availability

The data supporting the findings of this study are not publicly available but are available from the corresponding author upon reasonable request.

Supplementary information (SI) is available. The Supplementary Information file contains Supplementary Tables S1 and S2 reporting Euclidean distance analyses between control and treatment groups in the LDA score space, as well as ANOVA and Tukey post hoc comparisons among treatment groups. See DOI: https://doi.org/10.1039/d6fo00178e.

Acknowledgements

This work was also supported by a grant from the University of Florence (Fondi di Ateneo 2022–2024 awarded to Monica Bucciantini). M. L. was supported by Fondazione Umberto Veronesi (2021–2025). We also acknowledge support from the Italian Ministry of University and Research (MUR, formerly MIUR) through the "Dipartimenti di Eccellenza 2023–2027" program awarded to the Department of Experimental and Clinical Biomedical Sciences "Mario Serio".

References

1 M. G. Cersosimo and E. E. Benarroch, Estrogen actions in the nervous system: Complexity and clinical implications, *Neurology*, 2015, **85**, 263–273.
2 S. Arjmand, M. Ilaghi, A. K. Sisakht, M. B. Guldager, G. Wegener, A. M. Landau and A. Gjedde, Regulation of mitochondrial dysfunction by estrogens and estrogen receptors in Alzheimer's disease: A focused review, *Basic Clin. Pharmacol. Toxicol.*, 2024, **135**, 115–132.
3 M. Fiocchetti, P. Ascenzi and M. Marino, Neuroprotective effects of 17b-estradiol rely on estrogen receptor membrane initiated signals, *Front. Physiol.*, 2012, **3**, 73.
4 C. A. Finney, A. Shvetcov, R. F. Westbrook, N. M. Jones and M. J. Morris, The role of hippocampal estradiol in synaptic plasticity and memory: A systematic review, *Front. Neuroendocrinol.*, 2020, **56**, 100818.
5 K. M. Lenz, B. M. Nugent and M. M. McCarthy, Sexual differentiation of the rodent brain: dogma and beyond, *Front. Neurosci.*, 2012, **6**, 26.
6 M. M. Adams, S. E. Fink, W. G. Janssen, R. A. Shah and J. H. Morrison, *J. Comp. Neurol.*, 2004, **474**, 419–426.

7 N. Fuentes and P. Silveyra, Estrogen receptor signaling mechanisms, *Adv. Protein Chem. Struct. Biol.*, 2019, **116**, 135–170.
8 B. P. Kenealy, K. L. Keen and E. Terasawa, Rapid action of estradiol in primate GnRH neurons: the role of estrogen receptor alpha and estrogen receptor beta, *Steroids*, 2011, **76**, 861–866.
9 D. P. Srivastava, K. M. Woolfrey, F. Liu, N. J. Brandon and P. Penzes, Estrogen receptor ß activity modulates synaptic signaling and structure, *J. Neurosci.*, 2010, **30**, 13454–13460.
10 L. Carlstrom, Z. J. Ke, J. R. Unnerstall, R. S. Cohen and S. C. Pandey, Estrogen modulation of the cyclic AMP response element-binding protein pathway. Effects of long-term and acute treatments, *Neuroendocrinology*, 2001, **74**, 227–243.
11 L. C. Sheldahl, R. A. Shapiro, D. N. Bryant, I. P. Koerner and D. M. Dorsa, Estrogen induces rapid translocation of estrogen receptor beta, but not estrogen receptor alpha, to the neuronal plasma membrane, *Neuroscience*, 2008, **153**, 751–761.
12 W. Zhao, Y. Hou, Q. Zhang, H. Yu, M. Meng, H. Zhang and Y. Zhou, Estrogen receptor β exerts neuroprotective effects by fine-tuning mitochondrial homeostasis through NRF1/PGC-1α, *Neurochem. Int.*, 2023, 105636.
13 Z. Koszegi and R. Y. Cheong, Targeting the non-classical estrogen pathway in neurodegenerative diseases and brain injury disorders, *Front. Endocrinol.*, 2022, **13**, 999236.
14 A. Quesada, B. Y. Lee and P. E. Micevych, PI3 kinase/Akt activation mediates estrogen and IGF-1 nigral DA neuronal neuroprotection against a unilateral rat model of Parkinson's disease, *Dev. Neurobiol.*, 2008, **68**, 632–644.
15 C. M. Klinge, Estrogenic control of mitochondrial function, *Redox Biol.*, 2020, **31**, 101435.
16 L. Vinklarova, M. Schmidt, O. Benek, K. Kuca, F. Gunn-Moore and K. Musilek, Friend or enemy? Review of 17b-HSD10 and its role in human health or disease, *J. Neurochem.*, 2020, **155**, 231–249.
17 C. J. Pike, Sex and the development of Alzheimer's disease, *J. Neurosci. Res.*, 2017, **95**, 671–680.
18 E. L. Scott, Q. G. Zhang, R. K. Vadlamudi and D. W. Brann, Premature menopause and risk of neurological disease: basic mechanisms and clinical implications, *Mol. Cell. Endocrinol.*, 2014, **389**, 2–6.
19 P. Stute, J. Wienges, A. S. Koller, C. Giese, W. Wesemüller, H. Janka and S. Baumgartner, Cognitive health after menopause: Does menopausal hormone therapy affect it?, *Best Pract. Res. Clin. Endocrinol. Metab.*, 2021, **35**, 101565.
20 M. M. Alshehri, J. Sharifi-Rad, J. Herrera-Bravo, E. L. Jara, L. A. Salazar, D. Kregiel, Y. Uprety, M. Akram, M. Iqbal, M. Martorell, M. Torrens-Mas, D. G. Pons, S. D. Daştan, N. Cruz-Martins, F. A. Ozdemir, M. Kumar and W. C. Cho, Therapeutic Potential of Isoflavones with an Emphasis on Daidzein, *Oxid. Med. Cell. Longevity*, 2021, **2021**, 6331630.
21 S. Ronchetti, F. Labombarda, J. Del Core, P. Roig, A. F. De Nicola and L. Pietranera, The phytoestrogen genistein improves hippocampal neurogenesis and cognitive impairment and decreases neuroinflammation in an animal model of metabolic syndrome, *J. Neuroendocrinol.*, 2025, **37**, e13480.
22 C. Antoniou and J. Hull, The Anti-cancer Effect of Olea europaea L. Products: a Review, *Curr. Nutr. Rep.*, 2021, **10**, 99–124.
23 M. Leri, M. Scuto, M. L. Ontario, V. Calabrese, E. J. Calabrese, M. Bucciantini and M. Stefani, Healthy Effects of Plant Polyphenols: Molecular Mechanisms, *Int. J. Mol. Sci.*, 2020, **21**(4), 1250.
24 M. Leri, A. Bertolini, M. Stefani and M. Bucciantini, EVOO Polyphenols Relieve Synergistically Autophagy Dysregulation in a Cellular Model of Alzheimer's Disease, *Int. J. Mol. Sci.*, 2021, **22**(13), 7225.
25 M. Leri, M. Vasarri, F. Carnemolla, F. Oriente, S. Cabaro, M. Stio, D. Degl'Innocenti, M. Stefani and M. Bucciantini, EVOO Polyphenols Exert Anti-Inflammatory Effects on the Microglia Cell through TREM2 Signaling Pathway, *Pharmaceuticals*, 2023, **16**(7), 933.
26 M. Jordán, N. García-Acosta, J. L. Espartero, L. Goya and R. Mateos, Hydroxytyrosol Bioavailability: Unraveling Influencing Factors and Optimization Strategies for Dietary Supplements, *Nutrients*, 2025, **17**(18), 2937.
27 M. de Bock, E. B. Thorstensen, J. G. Derraik, H. V. Henderson, P. L. Hofman and W. S. Cutfield, Human absorption and metabolism of oleuropein and hydroxytyrosol ingested as olive (Olea europaea L.) leaf extract, *Mol. Nutr. Food Res.*, 2013, **57**(11), 2079–2085.
28 C. Angeloni, M. Malaguti, M. C. Barbalace and S. Hrelia, Bioactivity of Olive Oil Phenols in Neuroprotection, *Int. J. Mol. Sci.*, 2017, **18**(11), 2230.
29 C. Bender, S. Strassmann and C. Golz, Oral Bioavailability and Metabolism of Hydroxytyrosol from Food Supplements, *Nutrients*, 2023, **15**(2), 325.
30 L. Fan, Y. Peng and X. Li, Brain regional pharmacokinetics of hydroxytyrosol and its molecular mechanism against depression assessed by multi-omics approaches, *Phytomedicine*, 2023, **112**, 154712.
31 S. Rigacci, V. Guidotti, M. Bucciantini, M. Parri, C. Nediani, E. Cerbai, M. Stefani and A. Berti, Oleuropein aglycon prevents cytotoxic amyloid aggregation of human amylin, *J. Nutr. Biochem.*, 2010, **21**, 726–735.
32 M. Leri, A. Natalello, E. Bruzzone, M. Stefani and M. Bucciantini, Oleuropein aglycone and hydroxytyrosol interfere differently with toxic Aβ1–42 aggregation, *Food Chem. Toxicol.*, 2019, **129**, 1–12.
33 Q. Meng, Y. Chao, S. Zhang, X. Ding, H. Feng, C. Zhang, B. Liu, W. Zhu, Y. Li, Q. Zhang, H. Tong, L. Wu and H. Bian, Attenuation of estrogen and its receptors in the post-menopausal stage exacerbates dyslipidemia and leads to cognitive impairment, *Mol. Brain*, 2023, **16**(1), 80.
34 A. J. Valente, L. A. Maddalena, E. L. Robb, F. Moradi and J. A. Stuart, A simple ImageJ macro tool for analyzing mitochondrial network morphology in mammalian cell culture, *Acta Histochem.*, 2017, **119**, 315–326.
35 G. Fani, B. Mannini, G. Vecchi, R. Cascella, C. Cecchi, C. M. Dobson, M. Vendruscolo and F. Chiti, Aβ Oligomers

Dysregulate Calcium Homeostasis by Mechanosensitive Activation of AMPA and NMDA Receptors, *ACS Chem. Neurosci.*, 2021, **12**, 766–781.

36 J. Schindelin, I. Arganda-Carreras, E. Frise, V. Kaynig, M. Longair, T. Pietzsch, S. Preibisch, C. Rueden, S. Saalfeld, B. Schmid, J. Y. Tinevez, D. J. White, V. Hartenstein, K. Eliceiri, P. Tomancak and A. Cardona, FiJi: an open-source platform for biological-image analysis, *Nat. Methods*, 2012, **9**, 676–682.

37 I. Kondofersky, F. J. Theis, T. Hastie, R. Tibshirani and M. Wainwright, Statistical Learning with Sparsity: The Lasso and Generalizations, in *Biometrics*, CRC Press, Boca Raton, 2018.

38 F. Mosteller and J. Tukey, in *Revised Handbook of Social Psychology*, ed. G. Lindzey and E. Aronson, Addison Wesley, 1968, vol. 2, pp. 80–203.

39 D. Ami, A. R. Franco, V. Artusa, A. Romerio, M. M. Shaik, A. Italia, J. Anguita, S. Pasco, P. Mereghetti, F. Peri and A. Natalello, Vibrational spectroscopy coupled with machine learning sheds light on the cellular effects induced by rationally designed TLR4 agonists, *Talanta*, 2024, **275**, 126104.

40 L. Breiman, J. H. Friedman, R. A. Olshen and C. J. Stone, Classification and Regression Trees, *Biometrics*, 1984, **40**, 874.

41 B. G. Tabachnick and L. S. Fidell, *Using Multivariate Statistics*, Pearson Education, 2013.

42 M. M. Bradford, A rapid and sensitive method for the quantitation of microgram quantities of protein utilizing the principle of protein-dye binding, *Anal. Biochem.*, 1976, **72**, 248–254.

43 M. C. Tsai, S. H. Lin, K. Hidayah and C. I. Lin, Equol Pretreatment Protection of SH-SY5Y Cells against Aβ (25–35)-Induced Cytotoxicity and Cell-Cycle Reentry via Sustaining Estrogen Receptor Alpha Expression, *Nutrients*, 2019, **11**(10), 2356.

44 K. Saito and H. Cui, Emerging Roles of Estrogen-Related Receptors in the Brain: Potential Interactions with Estrogen Signaling, *Int. J. Mol. Sci.*, 2018, **19**(4), 1091.

45 T. W. Wu, S. Chen and R. D. Brinton, Membrane estrogen receptors mediate calcium signaling and MAP kinase activation in individual hippocampal neurons, *Brain Res.*, 2011, 34–43.

46 C. C. Smith and L. L. McMahon, Estrogen-induced increase in the magnitude of long-term potentiation occurs only when the ratio of NMDA transmission to AMPA transmission is increased, *J. Neurosci.*, 2005, **25**, 7780–7791.

47 C. J. Cookman and S. M. Belcher, Estrogen Receptor-β Up-Regulates IGF1R Expression and Activity to Inhibit Apoptosis and Increase Growth of Medulloblastoma, *Endocrinology*, 2015, **156**, 2395–2408.

48 G. P. Cardona-Gómez, P. Mendez, L. L. DonCarlos, I. Azcoitia and L. M. Garcia-Segura, Interactions of estrogens and insulin-like growth factor-I in the brain: implications for neuroprotection, *Brain Res. Brain Res. Rev.*, 2001, **37**, 320–334.

49 K. Yang, Z. Chen, J. Gao, W. Shi, L. Li, S. Jiang, H. Hu, Z. Liu, D. Xu and L. Wu, The Key Roles of GSK-3β in Regulating Mitochondrial Activity, *Cell. Physiol. Biochem.*, 2017, **44**, 1445–1459.

50 C. M. Klinge, Estrogenic control of mitochondrial function and biogenesis, *J. Cell. Biochem.*, 2008, **105**, 1342–1351.

51 T. L. Liao, C. R. Tzeng, C. L. Yu, Y. P. Wang and S. H. Kao, Estrogen receptor-β in mitochondria: implications for mitochondrial bioenergetics and tumorigenesis, *Ann. N. Y. Acad. Sci.*, 2015, **1350**, 52–60.

52 S. Y. Yang, X. Y. He and D. Miller, HSD17b10: a gene involved in cognitive function through metabolism of isoleucine and neuroactive steroids, *Mol. Genet. Metab.*, 2007, **92**, 36–42.

53 H. L. Casal and H. H. Mantsch, Polymorphic phase behaviour of phospholipid membranes studied by infrared spectroscopy, *Biochim. Biophys. Acta*, 1984, **779**, 381–401.

54 L. K. Tamm and S. A. Tatulian, Infrared spectroscopy of proteins and peptides in lipid bilayers, *Q. Rev. Biophys.*, 1997, **30**, 365–429.

55 A. Barth, Infrared spectroscopy of proteins, *Biochim. Biophys. Acta*, 2007, **1767**, 1073–1101.

56 M. Kacuráková and M. Mathlouthi, FTIR and laser-Raman spectra of oligosaccharides in water: characterization of the glycosidic bond, *Carbohydr. Res.*, 1996, **284**, 145–157.

57 M. Banyay, M. Sarkar and A. Gräslund, A library of IR bands of nucleic acids in solution, *Biophys. Chem.*, 2003, **104**, 477–488.

58 C. Petibois, A. M. Melin, A. Perromat, G. Cazorla and G. Déléris, Glucose and lactate concentration determination on single microsamples by Fourier-transform infrared spectroscopy, *J. Lab. Clin. Med.*, 2000, **135**, 210–215.

59 F. S. Parker, *Applications of infrared spectroscopy in biochemistry, biology, and medicine*, Plenum Press, New York, 1st edn, 1971.

60 H. Akutsu, Structure and dynamics of phospholipids in membranes elucidated by combined use of NMR and vibrational spectroscopies, *Biochim. Biophys. Acta. Biomembr.*, 2020, **1862**, 183352.

61 M. Kačuráková, P. Capek, V. Sasinková, N. Wellner and A. Ebringerová, FT-IR study of plant cell wall model compounds: Pectic polysaccharides and hemicelluloses, *Carbohydr. Polym.*, 2000, **43**, 195–203.

62 F. Sohrabji, Estrogen-IGF-1 interactions in neuroprotection: ischemic stroke as a case study, *Front. Neuroendocrinol.*, 2015, **36**, 1–14.

63 H. Tang, Y. Liao, L. Xu, C. Zhang, Z. Liu, Y. Deng, Z. Jiang, S. Fu, Z. Chen and S. Zhou, Estrogen and insulin-like growth factor 1 synergistically promote the development of lung adenocarcinoma in mice, *Int. J. Cancer*, 2013, **133**, 2473–2482.

64 M. Lagouge, C. Argmann, Z. Gerhart-Hines, H. Meziane, C. Lerin, F. Daussin, N. Messadeq, J. Milne, P. Lambert, P. Elliott, B. Geny, M. Laakso, P. Puigserver and J. Auwerx, Resveratrol improves mitochondrial function and protects against metabolic disease by activating SIRT1 and PGC-1alpha, *Cell*, 2006, **127**, 1109–1122.

65 L. H. Do, R. T. Da Costa and M. E. Solesio, Effects of nutrients and diet on mitochondrial dysfunction: An opportunity for therapeutic approaches in human disease, *Nutrients*, 2025, **191**, 118493.

66 J. Viña, J. Escudero, M. Baquero, M. Cebrián, J. A. Carbonell-Asíns, J. E. Muñoz, E. Satorres, J. C. Meléndez, J. Ferrer-Rebolleda, M. D. P. Cózar-Santiago, J. M. Santabárbara-Gómez, M. Jové, R. Pamplona, F. J. Tarazona-Santabalbina and C. Borrás, Genistein effect on cognition in prodromal Alzheimer's disease patients. The GENIAL clinical trial, *Alzheimers. Res. Ther.*, 2022, **14**, 164.

67 J. Li, S. Dong, S. Quan, S. Ding, X. Zhou, Y. Yu, Y. Wu, W. Huang, Q. Shi and Q. Li, Nuciferine reduces inflammation induced by cerebral ischemia-reperfusion injury through the PI3K/Akt/NF-κB pathway, *Phytomedicine*, 2024, **125**, 155312.

68 X. Zhu, R. Hao, X. Lv, J. Su, D. Li and C. Zhang, Neuroprotective effects of nuciferine on high-fat diet-induced cognitive dysfunction in obese mice: Role of insulin resistance, neuroinflammation, and oxidative stress, *Food Front.*, 2024, **5**, 833–844.

69 B. J. Connell, K. M. Crosby, M. J. Richard, M. B. Mayne and T. M. Saleh, Estrogen-mediated neuroprotection in the cortex may require NMDA receptor activation, *Neuroscience*, 2007, **146**, 160–169.

70 A. Ruiz, C. Matute and E. Alberdi, Intracellular Ca^{2+} release through ryanodine receptors contributes to AMPA receptor-mediated mitochondrial dysfunction and ER stress in oligodendrocytes, *Cell Death Dis.*, 2010, **1**, e54.

71 Z. Zhang, Z. He, J. Pan, M. Yuan, Y. Lang, X. Wei and C. Zhang, The interaction of BDNF with estrogen in the development of hypertension and obesity, particularly during menopause, *Front. Endocrinol.*, 2024, **15**, 1384159.

72 M. A. Silva-Soto, P. Carrillo-Fernández, E. T. Saez Lancellotti, E. Medina-Jiménez, J. F. Mogaburo Alba, N. Catena-Granados, M. D. López-Carmona, L. M. Pérez-Belmonte, N. Prieto Lain, A. I. Gómez Hernández, R. Gómez-Huelgas and M. R. Bernal-López, Extra Virgin Olive Oil Phenolic Compounds: Modulating Mitochondrial Function and Protecting Against Chronic Diseases-A Narrative Review, *Nutrients*, 2025, **17**(9), 1443.

73 S. Du Yan, Y. Zhu, E. D. Stern, Y. C. Hwang, O. Hori, S. Ogawa, M. P. Frosch, E. S. Connolly, R. McTaggert, D. J. Pinsky, S. Clarke, D. M. Stern and R. Ramasamy, Amyloid beta -peptide-binding alcohol dehydrogenase is a component of the cellular response to nutritional stress, *J. Biol. Chem.*, 2000, **275**, 27100–27109.

74 K. Zymone, R. Benetis, D. Trumbeckas, I. Baseviciene and S. Trumbeckaite, Different Effects of Quercetin Glycosides and Quercetin on Kidney Mitochondrial Function-Uncoupling, Cytochrome C Reducing and Antioxidant Activity, *Molecules*, 2022, **27**(19), 6377.

75 L. Almeida, M. Vaz-da-Silva, A. Falcão, E. Soares, R. Costa, A. I. Loureiro, C. Fernandes-Lopes, J. F. Rocha, T. Nunes, L. Wright and P. Soares-da-Silva, Pharmacokinetic and safety profile of trans-resveratrol in a rising multiple-dose study in healthy volunteers, *Mol. Nutr. Food Res.*, 2009, **53**(Suppl 1), S7–15.

76 G. Gherardi, A. Weiser, F. Bermont, E. Migliavacca, B. Brinon, G. E. Jacot, A. Hermant, M. Sturlese, L. Nogara, F. Vascon, A. De Mario, A. Mattarei, E. Garratt, M. Burton, K. Lillycrop, K. M. Godfrey, L. Cendron, D. Barron, S. Moro, B. Blaauw, R. Rizzuto, J. N. Feige, C. Mammucari and U. De Marchi, Mitochondrial calcium uptake declines during aging and is directly activated by oleuropein to boost energy metabolism and skeletal muscle performance, *Cell Metab.*, 2025, **37**(477–495), e411.

